CHALMERS
UNIVERSITY OF TECHNOLOGY

The effect of pore geometry on the mechanical properties of cast aluminium

Master's thesis in Applied Mechanics

Authors
BENJAMIN CORIC
SEYEDMAHDI SEYEDRAOUFI

DEPARTMENT OF INDUSTRIAL AND MATERIALS SCIENCE
CHALMERS UNIVERSITY OF TECHNOLOGY
Gothenburg, Sweden 2024
www.chalmers.se

Master's thesis 2024

The effect of pore geometry on the mechanical properties of cast aluminium

BENJAMIN CORIC
SEYEDMAHDI SEYEDRAOUFI

CHALMERS
UNIVERSITY OF TECHNOLOGY

Department of Industrial and Materials Science
Division of Material and Computational Mechanics
Chalmers University of Technology
Gothenburg, Sweden 2024

The effect of pore geometry on the mechanical properties of cast aluminium
BENJAMIN CORIC
SEYEDMAHDI SEYEDRAOUFI

Supervisor: Adj. prof. Renaud Gutkin, Volvo Cars Corporation. Department of Industrial and Materials Science, Chalmers University of Technology.
Examiner: Prof. Magnus Ekh, Department of Industrial and Materials Science

Master's Thesis 2024
Department of Industrial and Materials Science
Division of Material and Computational Mechanics
Chalmers University of Technology
SE-412 96 Gothenburg
Telephone +46 31 772 1000

Cover: Illustration of component that can be made from the mega casting project at Volvo Cars.

Typeset in LaTeX
Printed by Chalmers Reproservice
Gothenburg, Sweden 2024

The effect of pore geometry on the mechanical properties of cast aluminium
Benjamin Coric
Seyedmahdi Seyedraoufi
Department of Industrial and Materials Science
Chalmers University of Technology

Abstract

This thesis delves into the influence of pore geometry on the mechanical characteristics of High Pressure Die Cast (HPDC) aluminum. Additionally, it explores the feasibility of developing a material model capable of capturing the mechanical behavior for various types of porosity. Utilizing X-ray computed tomography Aided Engineering (XAE), pores were integrated into a virtual model, accurately mirroring those observed in the test coupons.
These virtual replicas, in conjunction with Representative Volume Element (RVE) models, were employed alongside Finite Element Methods (FEM) to simulate the effects of porosity, including variations in pore shape, volume, and distribution. Significant findings indicate that larger pores and those situated near boundaries substantially diminish both material strength and ductility.

An attempt was made to optimize the material model to encompass all findings from the test coupons. However, due to considerable disparities in failure strain among certain coupons, it was concluded that a single material model was inadequate for precise results. Consequently, two distinct material models were devised to address varying porosity volume fractions. The results demonstrate the potential for predicting failure in relation to porosity, with optimized models exhibiting a relatively accurate prediction of similar pore structures, with a maximum relative error of 6 % and 7 %, respectively.

Keywords: Porosity, Cast aluminium, RETOMO, LS-DYNA, GISSMO, FEM, Pore geometry, XAE, ANSA, Material characterisation.

Acknowledgements

We extend our heartfelt gratitude to our supervisor, Renaud Gutkin, for his invaluable introduction, guidance, and support throughout the project's duration. Our thanks also go to Johann Körbelin, whose consistent support and advice were pivotal every day of the project. A special mention to Stephan Esteki, whose assistance in data collection and enhancement was crucial to our project's success.
We are deeply appreciative of Prof. Magnus Ekh, our examiner, whose supportive discussions and insights were instrumental in advancing our project.
Lastly, our sincere thanks to Volvo Cars for enabling this master thesis by supplying essential resources like workspace, computers, and software. We are also grateful to the entire CAE Durability team for welcoming us and integrating us as part of their team.

Benjamin Coric & Seyedmahdi Seyedraoufi, Gothenburg, May 2024

Contents

List of Figures

List of Tables

1
Introduction

1.1 Background

High-pressure die-cast (HPDC) aluminum is increasingly employed in structural automotive applications due to its favorable mechanical properties, high efficiency, and the facilitation of producing complex-shaped thin-walled castings. Nevertheless, the HPDC method is notably influenced by diverse process parameters such as melt temperature, die temperature, pressure, velocity of the plunger, etc [1], [2]. These factors contribute to notable variability in the local material properties of the produced components, primarily due to casting defects such as porosity, which arise during the high-speed turbulent form-filling process [2]. An example of how this porosity can look in a coupon can be seen in Figure 1.1.

To understand the impact of these defects on material properties, it is feasible to design coupons with varying degrees of defects and establish empirical relationships of the mechanical properties. However, such approaches are limited to specific types of loading and require extensive experimentation for each new load case, which is time-consuming and costly. Additionally, the geometry, placement, and size of pores cannot be precisely controlled, making it rare to have coupons with identical porosity characteristics to study all aspects of porosity experimentally.

As a result, developing a virtual model is advantageous, as it is more efficient and allows for the exploration and evaluation of various scenarios. Thus, analyzing whether this can be achieved through a virtual model would be highly beneficial. However, porosity affects material properties and behavior. Therefore, to develop a material model that can represent material behavior with random porosity, an extensive investigation into the effects of pores on the mechanical properties of HPDC aluminum using experimental data and computer tomography (CT) scans is necessary. Such modelling is for example used for biocomposites [3], although then a microscopic model of a composite was created. For creating the aluminium model there are some similarities, but more so it is the process that is similar and followed. For instance, Zhang et al.[4] has performed a similar study on HPDC aluminium casting, although with the Gurson-Tvergaard-Needleman (GTN) model to capture the effect of the pores and not modeled the pores explicitly which is the aim for this study. Choi et al.[5] created a virtual model with the porosity calibrated, however it was for HPDC magnesium instead of aluminium. Since the process is still very similar, it was used as a reference and guidance in this report.

Moreover, the effect of porosity has also been studied before, Lordan et al. [6], [7] and Cácares et al. [8] have studied the same mechanical properties although for alloys and not isotropic aluminium as in this report. Despite this the results should be similar in behaviour, therefore they were used as references during the project. Streck et al. [9] has studied the effect of the proximity of pores to each other, noting that pores within a certain distance can be considered as one. This significantly impacts the material properties and is beneficial for simplifying models and reducing computational time.

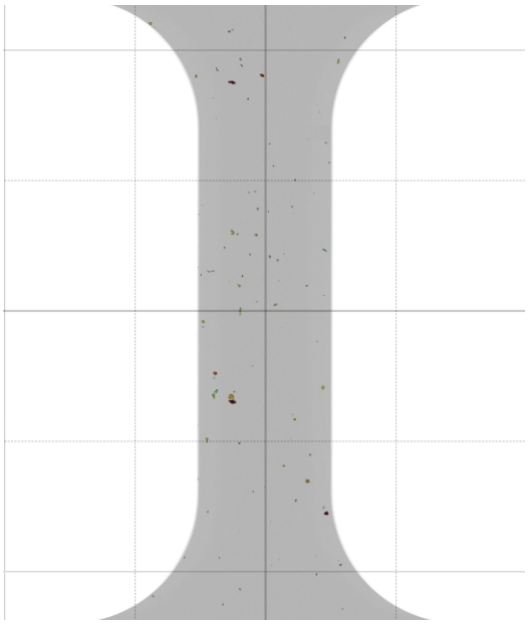

Figure 1.1: Porosity distribution in a coupon.

1.2 Objective

The main objective of this study is

- Develop a numerical model and using the Finite Element Method (FEM) for predicting the mechanical characteristics of porous cast aluminum.

Moreover, there is a supplementary goal along side the main objective, which is

- Study how the mechanical properties are influenced by varying pore geometry, including alterations in pore size, distribution, and volume fraction.

1.3 Limitations

Limitations are set on the project as to account for available resources in time and material.

- While various types of defects, including oxide, hot tear, cold shut, and others, may occur, this project exclusively concentrates on modeling the impact of porosity.
- Physical testing will not be conducted further unless deemed necessary. The primary model will be constructed using available data and CT scans.
- The properties of the aluminum alloy are regarded as an isotropic material, and observations will be made within the aluminium matrix domain.

2

Theory

In the following sections, the theory needed for executing the project will be presented. Some sections will be covered very broadly, whilst other, more important, sections will be covered more in depth.

2.1 High-pressure die-cast (HPDC)

In HPDC, molten metal or metal alloy is injected at high speed and high pressure into the mould. This is beneficial since it can produce very large light alloy parts in high volumes and great speeds as well as delivering light alloy parts with high precision, superior surface finish, excellent uniformity and optimum mechanical properties. Moreover, it is also useful for producing components with thin walls [10].

However, there are also some drawbacks with this production method as there are a number of defects that can occur. These defects form due to a range of mechanisms, such as oxidation, entrainment, incorporation of exogenous materials from the containment vessels, dissolved gasses, solidification shrinkage, unwanted microstructural phases with detrimental morphologies and the development of stresses in the solidifying metal [11]. The main defect formed, is that porosity occurs within the part, which can give significant impact on the mechanical properties.

When it comes to HPDC, there are mainly two types of porosity that are generated: shrinkage porosity and gas porosity. Solidification porosity is caused by the density in change from liquid to solid during solidification which is formed when the shrinkage can no longer be fed by flow of the liquid. This often occurs late in the solidification, when the solid dendritic network has a low permeability and is rigid. Consequently, the porosity gets a tortuous shape of the remaining spaces between the dendrites [12].

Gas porosity, on the other hand, occurs when the molten alloy contains relatively large amounts of a dissolved gas. In this instance, pores can form much earlier in solidification, and therefore, the pores have the freedom to adopt a more spherical shape [12].

2.2 X-ray computer tomography scanning

X-ray computer tomography was originally used within the medical field in the 1960s but was later extended to use in both non-medical research and industry [13]. This was adapted into an engineering tool and is also referred to as X-ray computer tomography aided engineering (XAE).
To obtain a 3D model, the sample is turned around itself and exposed to the X-ray beam from different angles to obtain as many 2D projections as possible [13]. After acquiring the images, a segmentation needs to be applied to differentiate the different objects within the coupon. The segmentation is done by grey-scale thresholds for the two different parts, voids (pores) and matrix (aluminium).

A greyscale image is one where each pixel is representing an amount of light, where black represents the weakest amount of light and white the highest. Most images have values somewhere in between giving them a grey look and therefore the name greyscale. The "color" value of these pixels is easiest seen in a histogram, see Figure 2.1, where the x axis shows the different values for the coloring (from black to white) and the y axis shows the amount of pixels there are for a specific value. In the histogram there will then be peak values that indicate the different parts/objects. Here a threshold is implemented to distinguish the different materials and it is often done at the minimum value between the peaks of the histogram, as shown in Figure 2.1.

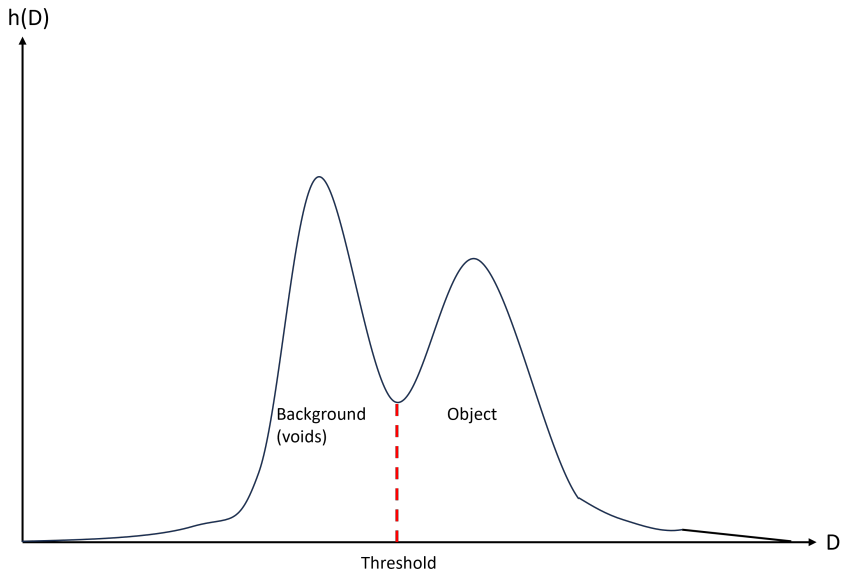

Figure 2.1: An example of threshold determination from a histogram of image data, inspired by [14].

2.3 RVE modeling

Representative Volume Element (RVE) is a volume of the material of a size large enough that the homogenized (averaged) properties becomes equal to volumes of an

increased size. Therefore it is often sought out to find the minimum possible size of the RVE since this will lead to the highest computational efficiency.

2.4 Material modeling

To ensure accurate results from the FEM model, it is essential to assign elements a suitable material model. In LS-DYNA this is employed through different "cards", where each card employs a unique attribute.

2.4.1 MAT_24

MAT_PIECEWISE_LINEAR_PLASTICITY or MAT_24 as it is more commonly known, is an elasto-plastic material with a given stress as a function of strain curve and arbitrary strain rate dependency [15]. This material card encompasses both linear elastic and plastic properties, and is used to model the behavior of the material up to the point of instability. For the elastic region, the essential parameters include Young's modulus, mass density, and Poisson's ratio, with the Von Mises yield criterion employed to identify the onset of plasticity. For the hardening phase, several options are available, such as linear hardening, where the yield strength, σ_y, and the tangent stiffness modulus, E_{tan}, are used. The yield strength defines the stress at which the material transitions from elastic to plastic deformation, while E_{tan} provides the linear hardening characteristic.

However, materials rarely exhibit linear hardening behavior. Therefore, employing a nonlinear hardening curve is more advantageous for accurately predicting material behavior. To achieve this, LS-DYNA provides several models, including Swift, Hockett-Sherby, Voce, and Gosh, which can describe isotropic hardening [15].

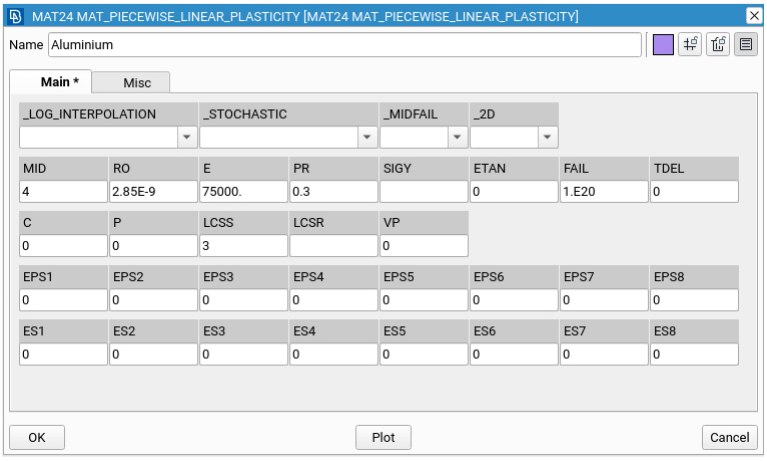

Figure 2.2: MAT_24_PIECEWISE_LINEAR_PLASTICITY card in ANSA.

2.4.2 Hockett-Sherby hardening curve/Hardening rule

A hardening rule is used to define the evolution of yield surface during a deformation process. Aluminium, like almost all other metals, increases its strength when being subjected to plastic deformation and this increase in yield strength leads to changes in the yield surface. This change due to plastic loading is called the hardening rule [16].

Generally the hardening behaviour is predicted using a hardening model or curve. The hardening models are mainly divided into two types, unbounded and saturation. The difference between an unbounded hardening model and a saturation hardening model lies in how they describe the behavior of materials under plastic deformation. In an unbounded model, a material can undergo limitless plastic strain without reaching a saturation threshold. The strain-hardening exponent, often represented as "n", defines the material's strain hardening during forming, calculated from the slope of the flow curve in a double-logarithmic format [17]. In contrast, a saturation hardening model suggests there is a threshold for a material's strain hardening. Beyond this saturation point, additional plastic deformation does not cause further hardening, as observed in materials like aluminum. In such cases, a saturation model, such as the Hockett-Sherby model is used. In LS-DYNA it is defined as:

$$\sigma = A - Be^{-C\epsilon_p^H}, \tag{2.1}$$

where A represents the yield stress, B stands for the difference between saturation stress and yield stress, C is a material constant that determines the rate of hardening, H indicates the strain hardening exponent, which describes how the hardening behavior changes with strain, and ϵ_p signifies the plastic strain [15]

2.4.3 GISSMO

As stated earlier, MAT_24 incorporates both linear elastic and plasticity behaviors, but the damage and failure behaviour is missing. Hence, an additional failure model

is necessary. GISSMO is employed for this purpose, and it can be applied by adding MAT_ADD_DAMAGE_GISSMO to the material model.
The basis of GISSMO is a damage evolution depending on a failure curve $\epsilon_f(\eta)$ where η is the stress triaxiality, which is further explained in section 2.4.3.2.

2.4.3.1 Damage Mechanics

Damage plays a pivotal role in material failure. It affects the material parameters and even small damage can have significant impact. The measure of damage, D, shows the change of the section area with damage compared with the reduced "effective" section area, see Figure 2.3, and is described as

$$D = \frac{S - \hat{S}}{S}. \tag{2.2}$$

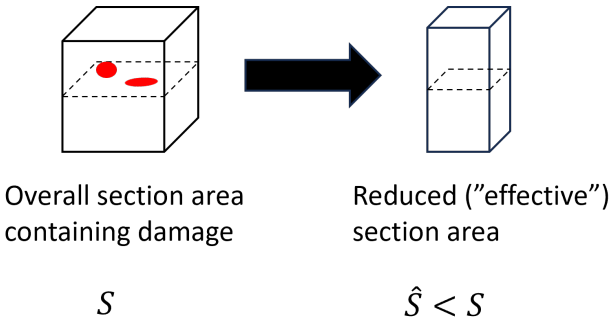

Figure 2.3: Visualization of damage measurement, reproduced from [18].

If $D = 1$ then failure occurs which is shown in eq.(2.3) where the effect of the damage on the true stress is shown. This is also commonly known as Lemaitres formulation [19] which is a relation to couple the damage to the stresses

$$\sigma_{true} = \sigma_{eff}(1 - D), \tag{2.3}$$

where σ_{eff} is the effective stress that is obtained in the reduced ("effective") section area, see Figure 2.3. Combining this with the treatment of material instability a damage threshold can be defined. When the damage parameter D reaches this value, it will cause damage and flow stress to become coupled [20]. After reaching necking, eq.(2.3) is altered and a value of critical damage, D_{crit}, is determined and implemented for the calculation of the effective stress tensor

$$\sigma_{true} = \sigma_{eff}\left(1 - \left(\frac{D - D_{crit}}{1 - D_{crit}}\right)^m\right), \text{ for } D \geq D_{crit}. \tag{2.4}$$

Additionally to the true stress, the damage accumulation rule plays a pivotal role in GISSMO, which is written as:

$$\Delta D = \frac{n}{\epsilon_f(\eta)} D^{1-\frac{1}{n}} \Delta\epsilon_p \tag{2.5}$$

where D is the damage, η is the triaxiality, $\Delta\epsilon_p$ is the increment of plastic strain and, n, the damage exponent [21]. This formula enables GISSMO to give a more accurate depiction of fracture for non-proportional stress paths [22]. For a constant value of the failure strain eq.(2.5) can be integrated and a relation of damage and actual equivalent plastic strain is obtained:

$$D = \left(\frac{\epsilon_p}{\epsilon_f}\right)^n. \tag{2.6}$$

Additionally, the instability accumulation can be defined as:

$$\Delta F = \frac{n}{\epsilon_{crit}(\eta)} F^{1-\frac{1}{n}} \Delta\epsilon_p \tag{2.7}$$

where F is the current value of instability and $\epsilon_{crit}(\eta)$ is the instability strain [21].

Understanding the physical implications of the two exponents (n and m) can be challenging as they are closely intertwined. Figures 2.4 and 2.5 illustrate the effects of the damage and fade exponents, respectively.

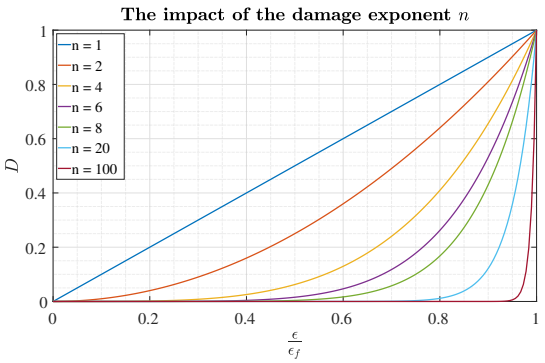

Figure 2.4: Effect of the damage exponent n.

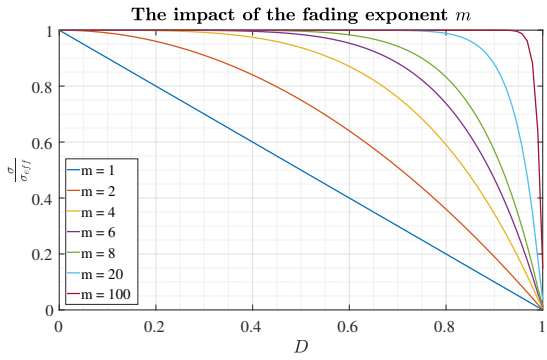

Figure 2.5: Effect of the fading exponent m.

It can be observed that the higher value of these variables, the "quicker" or more sudden the damage rises to 1 and failure occurs.

2.4.3.2 Stress triaxiality Curve

Stress Triaxiality, η, is an essential part of GISSMO as it is a part of the load curve needed to be implemented. Stress triaxiality is defined as the hydrostatic stress over the equivalent von Mises stress.

$$\eta = \frac{\sigma_m}{\sigma_{eq}}. \tag{2.8}$$

It is used to determine the failure of a material under different stress states, this is done by doing specific load cases for multiple coupons with the same properties until failure occurs. Some tests and the respective stress triaxiality values can be seen in Figure 2.6. Subsequently, by using these stress triaxiality values and corresponding plastic failure strains, a failure curve can be created. It is worth noting that in this report, the term "triaxiality" refers specifically to stress triaxiality.

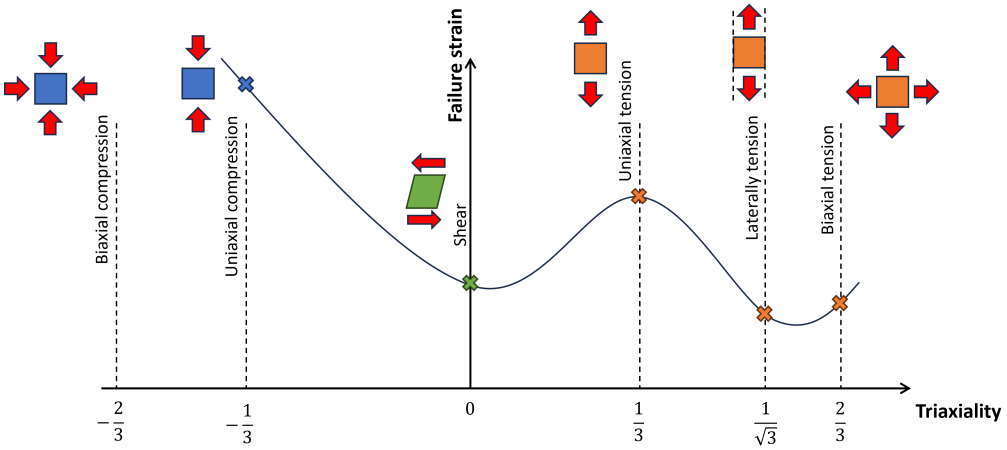

Figure 2.6: Plastic failure strain for different triaxiality, inspired from [23].

2.5 Material Calibration

In FEM, certain material parameters may be unknown. To ensure precise simulations and results that align with experimental data, it is crucial to calibrate the material model. Various software tools can be used for optimizing these parameters, such as LS-OPT.

To begin optimization, the force-displacement curve derived from experimental data serves as the reference. The previously prepared FE model is then simulated. Within this simulation, the points representing the extensometer in the real coupon are identified, and the force-displacement data from the simulation is extracted. Additionally, desired variables are designated as parameters. Using LS-OPT, the model undergoes simulation iterations, adjusting parameter values to minimize the error between the simulation and experiment. For this optimization, the Mean Square Error (MSE) function is employed. The formula for MSE is as follows:

$$MSE = \frac{1}{n}\sum_{n=1}^{n}(Y_i - \bar{Y_i})^2 \tag{2.9}$$

where Y_i is the estimated value points, $\bar{Y_i}$ is the actual value points and, n, is the number of data points. To globally minimize the error and avoid converging to local minima, it is crucial to set appropriate bounds for the parameters and provide a well-informed initial guess. Having a thorough understanding of the parameters leads to better, faster, and more accurate calibration [24].

3
Methodology

In this chapter, the methodology of the project will be presented. All the decisions taken will be highlighted along with motivations for the different chosen methods.

3.1 X-ray computer tomography aided engineering

This section outlines the X-ray computer tomography aided engineering process and its interpretation within this thesis project. The process consists of three main stages: image acquisition, segmentation, and meshing. However, due to constraints mentioned in the limitations section, the CT scans were already extracted by Volvo Cars prior to this thesis project. As a result, only the segmentation and meshing phases were performed in this study.

Segmentation and meshing phases were conducted utilizing the commercial software RETOMO from BETA CAE Systems. The input file necessary for analysis was in ".raw" format. Segmentation was a critical procedure aimed at modeling distinct phases such as void and matrix as separate materials. This segmentation was accomplished using the grey-scale threshold method, as detailed in Section 2.2.

In RETOMO, one has the option to mesh using surfaces or solids. For this thesis, a surface mesh elements was employed. Due to complex geometry of the pores, tetrahedral elements were chosen to mesh the coupon. Concerns about potentially missing shapes and very small pores led to the selection of the fine mesh option. Figure 3.1 illustrates the mesh extracted from RETOMO. Opting for the fine mesh option in RETOMO resulted in approximately 23 million extracted elements, leading to prolonged computational times.

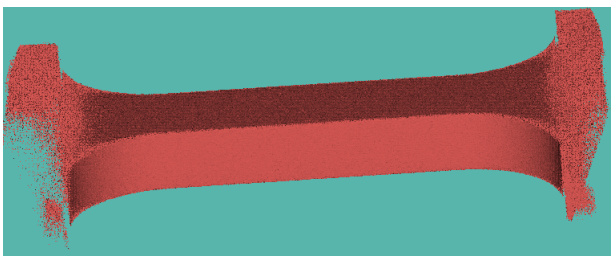

Figure 3.1: Extracted mesh from RETOMO.

3.2 FE-modelling

The procedure entailed developing a FE model using the ANSA software, which was based on the model prepared using RETOMO. Subsequently, the coupon with actual pores was prepared in ANSA along with additional pre-processing actions, i.e. applying boundary conditions. At the final stage, the model was run by using LS-DYNA explicitly.

3.2.1 Creating the geometry

The geometry created was a virtual replica of the standard coupon used in the mechanical test, which can be seen in Figure 3.2. The geometry was created directly in ANSA which made it easy to interact with the model for the extracted pores.

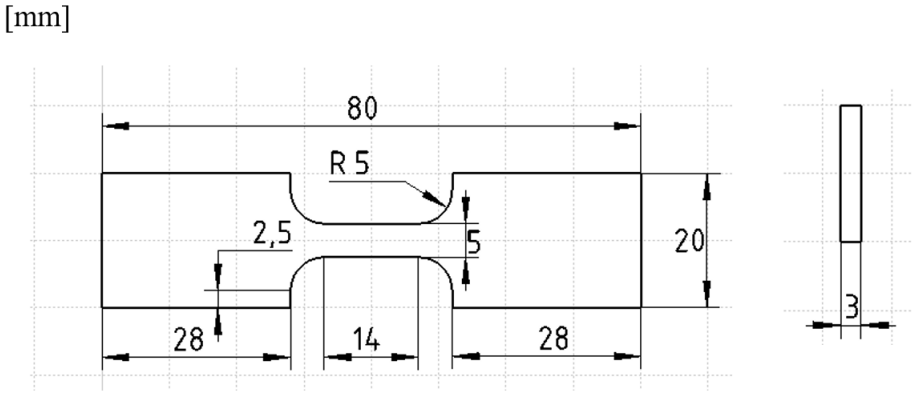

Figure 3.2: The geometry of the coupon used in the mechanical testing.

3.2.2 Meshing

As mentioned in section 3.1, a significant number of elements led to expensive computational time. Consequently, a decision was made to retain the surface mesh around the pores while deleting the remaining surface meshes. Subsequently, the previously prepared coupon model was meshed. Then the pores were subtracted from the coupon and finally, a coupon with real distribution of the pores was generated. This approach significantly reduced the overall number of elements and a visual representation of the procedure can be seen in Figure 3.3. Second order tetrahedral elements are recommended for simulating accurate fracture behaviors in this setup.

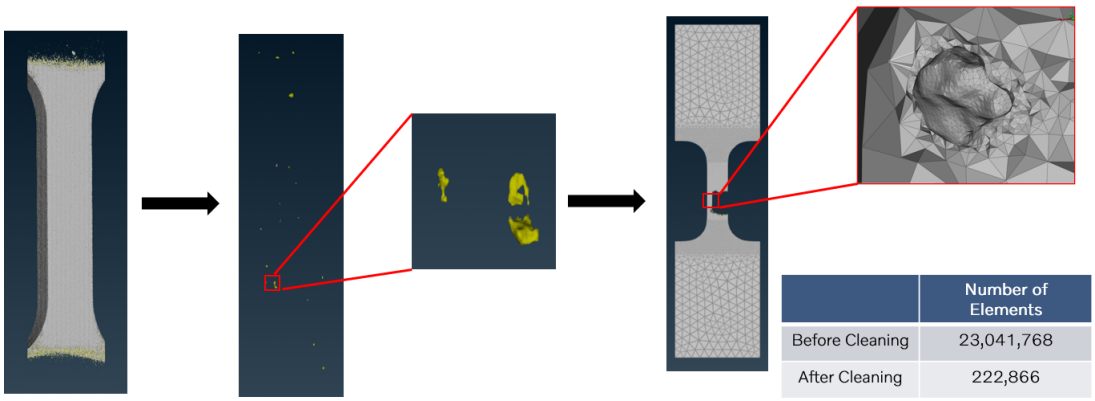

Figure 3.3: The process of creating a coupon with pores.

3.2.3 Material modelling

The material behavior was captured using a combination of MAT_24, the Hockett-Sherby function, and MAT_ADD_DAMAGE_GISSMO, allowing for representation of different sections such as linear elastic, hardening, and failure. Material parameters for the linear elastic and hardening sections are presented in Table 3.1. The plasticity part, a Hockett-Sherby hardening curve was implemented by applying a "Define_Curve_Stress" in LS-DYNA.

Table 3.1: Material parameters.

	Parameters			
Elasticity	E	ρ	ν	-
Plasticity and hardening	A	B	C	H
GISSMO failure	m	n	ϵ_{crit}	-

Implementing GISSMO failure was indeed more complicated than the initial two parts. This involved several material parameters (Table 3.1) as well as the failure curve.

As discussed in section 2.4.3, a GISSMO failure curve is typically derived from various tests like uniaxial tension, biaxial tension, pure shear, etc. With cast aluminum, each coupon's porosity varied, which led to different properties. Consequently, for the coupon, only a tensile test load case could be implemented in the GISSMO curve, as it was the mechanical test performed on it.

To address this constraint, two approaches were taken.For the initial failure curve, the average plastic failure strain (ϵ_{pf}) was derived from multiple tests conducted on cast aluminum data for each triaxiality.

Another approach considered was to utilize a failure curve obtained from a literature review for comparative analysis. To achieve this, an extensive review was conducted to select a failure curve that closely aligns with our experimental data [25]. The failure curve for both approaches are shown in Figure 3.4.

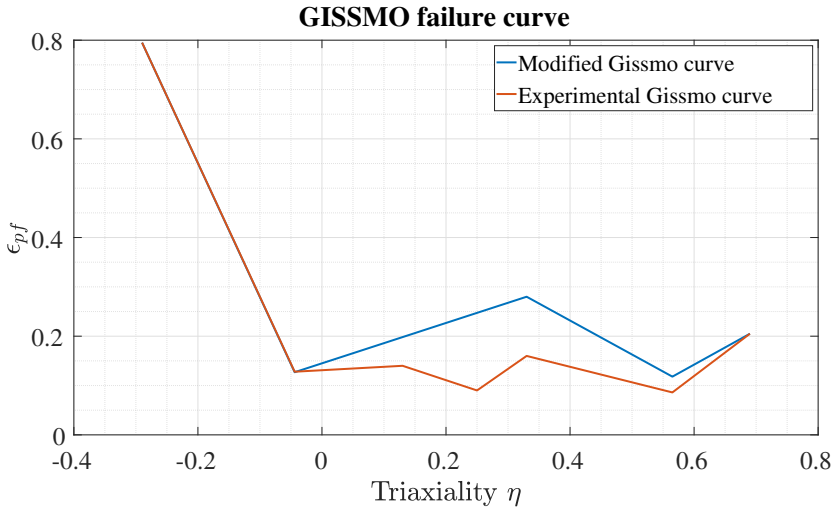

Figure 3.4: GISSMO failure curve from experimental data and literature.

3.3 Calibration

The calibration was divided into several steps, to ensure that each obtained variable was as independent and accurate as possible. Firstly the parameters for the Hockett-Sherby hardening curve were calibrated against experimental data to obtain the parameters A,B,C and H. To achieve a precise alignment with experimental data, the failure criterion was excluded to prevent any influence of failure damage on the results.

To calibrate the failure, various parameters like the damage exponent, n, and fading exponent, m, were chosen for calibration. Additionally, as discussed in sections 1.3 and 3.2.3, the failure curves obtained from section 3.2.3 were adjusted up and down until satisfactory experimental results were achieved. It is important to note that ϵ_{crit}, which represents the critical plastic failure strain, was derived from experimental data.

The optimization algorithm for a single coupon optimization is depicted in Figure 3.5.
In this project, five different coupons were used for optimization and to assess the performance of the calibrated material, three additional coupons were investigated. For each individual coupon, the same optimization algorithm shown in Figure 3.5 was employed to calibrate the material parameters and capture experimental data.

Upon examination of the CT scans, it was observed that coupon 1-4 had the biggest pore size among the selected coupons. Consequently, the simulation and optimization were initially conducted on this coupon. Moreover, to obtain material parameters applicable for different coupons, a parallel optimization was conducted, which is seen in Figure 3.6.

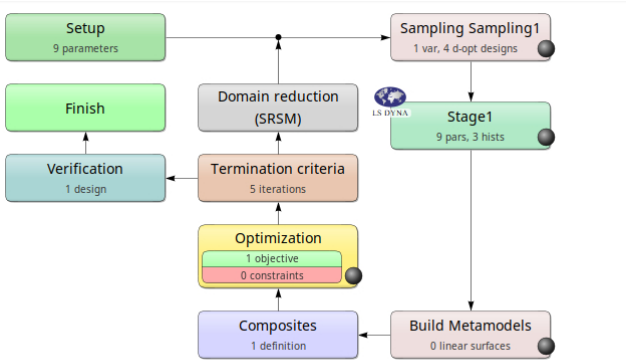

Figure 3.5: single optimization algorithm.

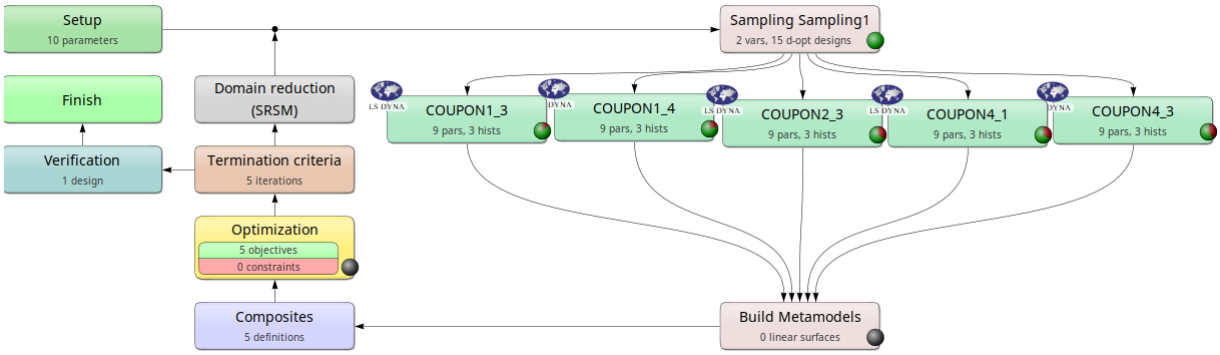

Figure 3.6: Multiple optimization algorithm.

3.4 Mesh regularization

The GISSMO failure model depends on the element size, meaning that different element sizes can yield varying results. To visualize this discrepancy caused by the element size, a study was conducted on mesh dependency. To ensure the model was independent of element size, the smallest possible element size was chosen as a reference. A simulation was then conducted using larger element sizes, and the failure curve was adjusted by a factor to align the results of the new simulation with those of the reference size. This procedure was repeated for different element sizes. In the final stage, a table or curve was generated to ensure that the GiSSMO failure curve was independent of element size.
Due to the necessity of capturing pore geometry, an element size of 0.01 mm was utilized in this study. However, for computational efficiency and to meet constraints for the subsequent stages, the element size in the middle of the coupon was around 0.5 mm. Consequently, the presence of porosity resulted in a mesh with varying sizes, ranging from 0.01 mm to 0.5 mm. Moreover, investigating the element size at 0.01 mm presented challenges, as it resulted in a model with millions of elements, making computation time intensive and costly. Additionally, tetrahedral elements were sensitive, and their element size computation logic differed from that of hexahedral elements. Therefore, to achieve a more uniform element length, it was preferable

to avoid geometry complexities such as curves. To address these limitations, a decision was made to study the effect of element size in a cube without any pores.
The boundary condition was configured such that one of the corner nodes at the bottom of the cube was fixed in translation in all directions. Additionally, all other nodes on the bottom were fixed in the vertical direction and free to translate in all other directions. On the top surface, a displacement of 3 mm was applied over a period of 0.01 seconds. This boundary condition setup was chosen to prevent the cube from being over-constrained, which could lead to inaccurate results.
It is also worth noting that the material model used for this regularization is divided into two parts. As shown in Figure 3.8, the material without any failure is assigned to the top and bottom parts of the cube, while the material model that includes failure is assigned to the middle of the cube (highlighted in purple).

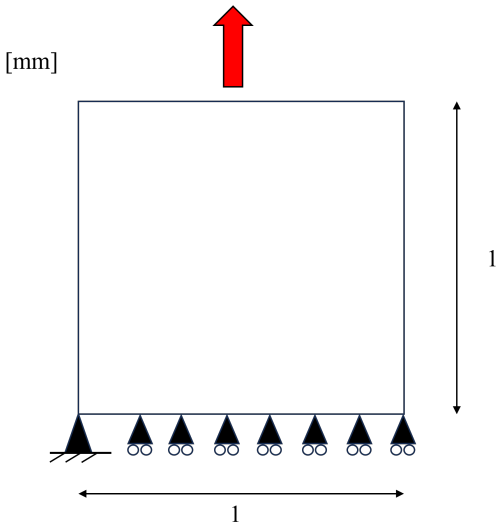

Figure 3.7: The boundary condition used for the mesh dependency study of the GISSMO failure curve.

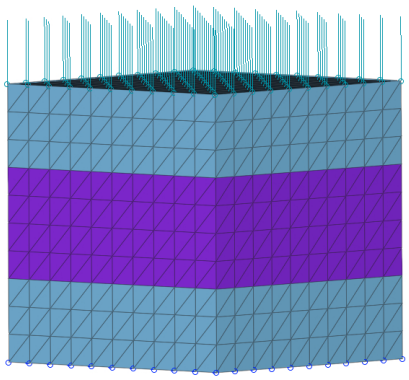

Figure 3.8: The material model used for the mesh dependency study of the GISSMO failure curve.

3.5 Pore geometry study

To comprehensively understand the effects of the pore geometry, which encompasses parameters such as shape, size, and placement, this study was divided into three distinct stages: shape analysis, size analysis, and placement analysis. This approach enabled a systematic examination of each parameter's individual impact without the risk of interfering effects.

3.5.1 Effect of pore shape on material behavior

For the purpose of studying the impact of pore geometry, an RVE model was initially created with the intention of using periodic boundary conditions. However, in LS-DYNA, periodic boundary conditions were only feasible for implicit simulations. Unfortunately, the implicit solution encountered difficulties in achieving convergence once failure was initiated, leading to unreliable results. To address this, some damping was introduced to better capture failure behavior, although this yielded only minimal improvement. Instead of pursuing periodic boundaries for the RVE, an alternative approach was taken, constructing a model similar to a coupon. This model was still a cube, similarly to the RVE, however the size was 10x10x10 mm^3, see Figure 3.9. The boundary conditions were similar to those used in the case with mesh regularization as described in section 3.4.

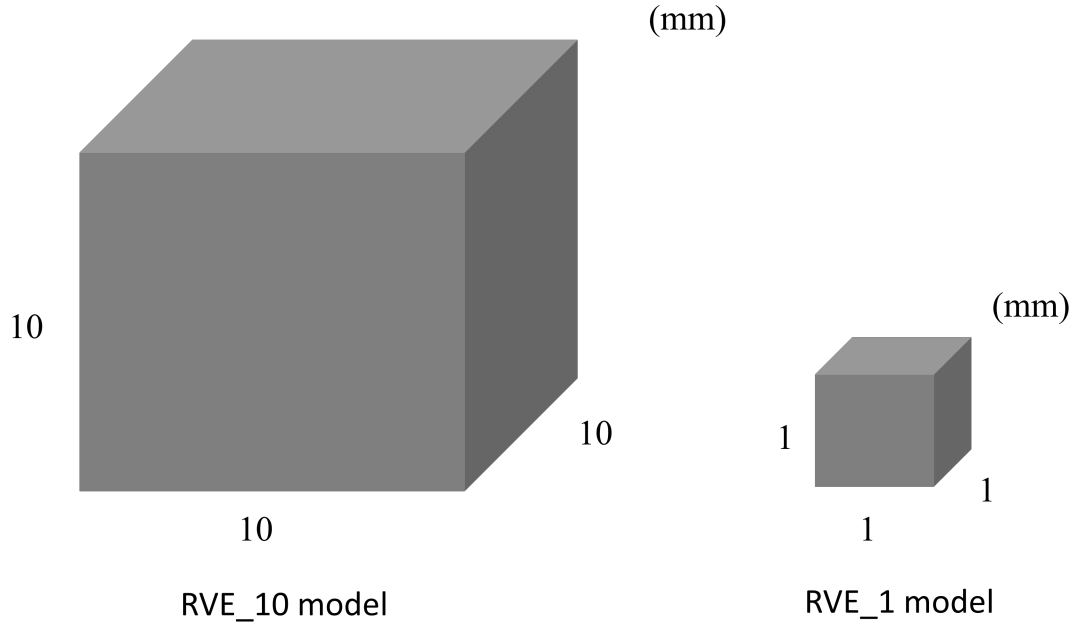

Figure 3.9: The two different RVE models used in the studies in section 3.5. The small RVE model is called RVE_1 whilst the model with similar size to the coupons is referenced as RVE_10.

In this model, different types of pore geometries were constructed, however, with one constant factor, which was that the volume fraction was always 0.5 %. The

different geometries that were analyzed are shown in Figure 3.10. The main shape analyzed was a spherical shape, although also ellipsoid shapes were examined as well as including a real pore from coupon 1-4. The goal was to both analyze how the different shapes of a pore behave, but also to see what has a greater impact, a few large pores or many smaller ones. Another thing of interest was to see the impact of the distance, both between the pores themselves but also the distance from the pore to the boundaries (the edges of the coupon).

The interest in the ellipsoid shape stemmed from its resemblance to the shape of a small crack initiation. Consequently, it allowed for visualization of its behavior under various loading conditions.
The reason for the spherical shape being the main one used was that it was considered to be the shape that was the least influential of the loading direction, since it had an universal radius. Additionally, it was considered to resemble the real pores quite well, and therefore it was considered that it would also capture the behaviour of the pores in the test coupons.
Lastly, also a large pore from the real coupon was chosen and scaled up, as to observe the difference in behaviour in comparison with the spherical and ellipsoid shaped pores.

To better understand and see the effect of the interpolar distance, a model with two pores, still with a volume fraction of about 0.5 %, was used. The pores were modeled as spheres with a radius of 0.84 mm each. The distance between the outer edges of the pores (the smallest distance between them) was altered from 0.32 mm to 1.32 mm, 3.32 mm and finally 4.32 mm. By starting from 0.32 mm, it also included the effect of the pores merging as according to Streck et al. [9], when the distance between two pores was less than the diameter of the smallest pore, they could be considered as one pore.

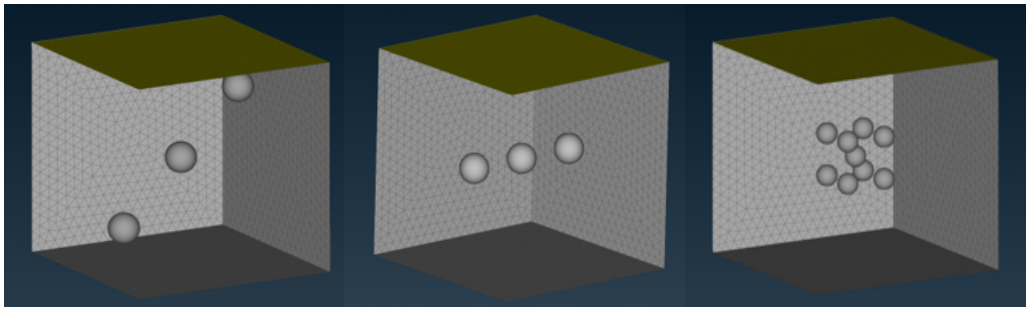

(a) Three spherical pores diagonal.

(b) Three spherical pores horizontally.

(c) 9 Pores clustered.

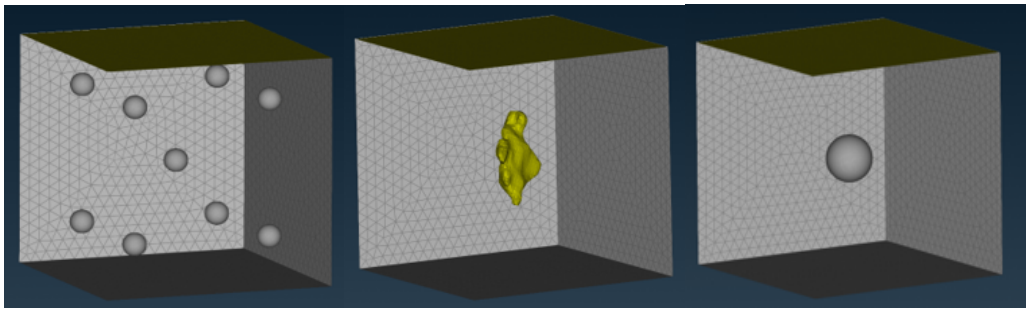

(d) 9 Pores spread out.

(e) Real pore form CT scan.

(f) Spherical pore.

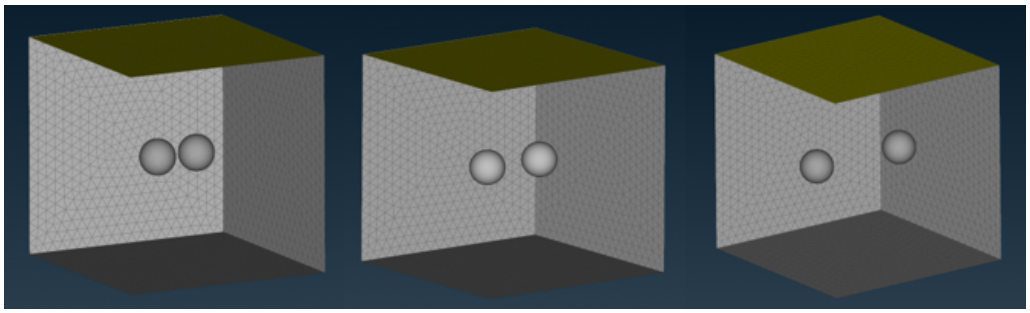

(g) Two spherical pores distanced 0.32 mm.

(h) Two spherical pores distanced 1.32 mm.

(i) Two spherical pores distanced 3.32 mm.

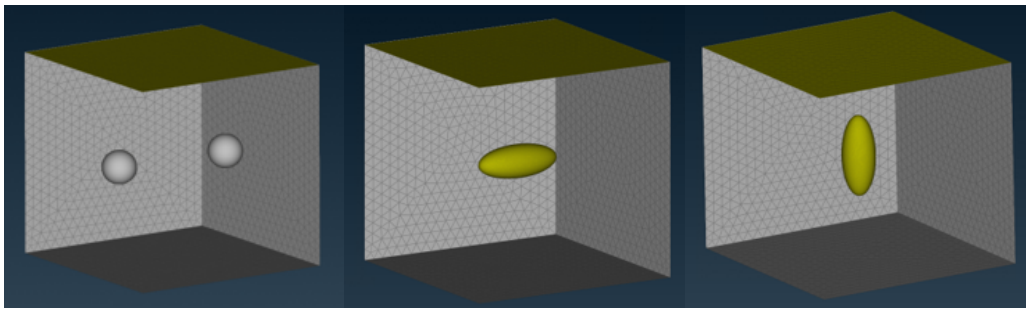

(j) Two spherical pores distanced 4.32 mm.

(k) Ellipsoid shaped pore, orthogonal to the loading direction.

(l) Ellipsoid shaped pore, parallel to the loading direction.

Figure 3.10: The different geometries that were analyzed. All the different models have a volume fraction of about 0.5 %.

3.5.2 Effect of pore volume on material behavior

The volume of pores had a notable impact on material behavior. Larger pores generally resulted in the material being weaker and more prone to brittleness. To visualize where this limit occurred a study on the pore volume fraction was performed and an RVE model consisting of a box with the dimensions 1x1x1 mm^3 was used (illustrated in Figure 3.9).

The tested pore sizes ranged from a volume of 0.0001 mm^3 to 0.005 mm^3, with a consistent spherical shape employed across all volumes. Additionally, to eliminate any potential discrepancies in results attributed to pore placement, the center of each pore was positioned at the center of the box.

The boundary conditions were set up as in the case with the mesh regularization, where one of the bottom node corners was fixed completely in translation and the other bottom nodes only fixed in translation in the loading direction (in this case in y-direction), see Figure 3.7 for a visualization. The loading was applied as a displacement of 1 mm over 0.01 seconds and the material and failure models were exactly the same as for coupon 1-4.

3.5.2.1 Effect of porosity on the ductility of the material

In addition to examining the failure strain, the RVE_1 model was used to assess the influence of pores on the ductile properties of the material, particularly on the parameter ϵ_{crit}, which denoted the onset of damage. Increasing this value implied that damage initiation occurred later, while the failure strain should remain the same, consequently, the ductility should decrease.

To observe this impact, the RVE_1 model was initially simulated using the ϵ_{crit} value obtained from coupon 1-4. Thereafter, the simulation was rerun with an elevated ϵ_{crit} value of 0.2. The pore was assumed to be spherical and its radius and respective volume is shown in Table 3.2. The pore sizes analyzed were chosen to be very small as to capture the smallest amount of pores required to observe the effect it has on the ductility.

Table 3.2: The pore volumes (and subsequential sphere radius) used for studying the effect of ϵ_{crit}.

	Radius (mm)					
	r=0	r=0.005	r=0.01	r=0.02	r=0.03	r=0.05
Pore Volume (mm^3)	0	5.24e-7	4.19e-6	3.35e-5	1.13e-4	5.24e-4

3.5.3 Effect of pore placement on material behavior

Additionally to considering the pore geometry, it was also necessary to consider its environment and its placement. Therefore a study was performed to analyze the

impact that the boundary had on the pore and the failure of the material. For this, the RVE_10 model was used since it had a similar size to the coupons. As the distance to the boundary was of interest here, the volume of the pore was set to a fixed value and shape, here chosen to be a sphere with a volume of 0.0015 mm^3. This volume was close to the average maximum pore size extracted from the coupons and therefore it was regarded as an accurate representative pore volume.

The way the boundary was then altered was by shifting the distance between the outer edge of the pore to the boundary on the right side. The initial distance was 5 mm, then 3 mm, 2 mm and finally 1 mm. Since the RVE_10 model was 10x10x10 mm^3, it meant that a distance of 5 mm was in the middle of the model and the furthest possible distance from one boundary. Moreover, the material model and the loading conditions were the same as for the volume studied in section 3.5.2.

4

Results

In this chapter, the results of the project will be presented, following the methodologies outlined in Chapter 3. Eight different coupons were studied and investigated in this project. These coupons were extracted from a prototype tool and can be observed in Figure 4.1.

The location of pores within the material structure plays a crucial role when determining its behavior. The flow stream initiates from the top, leading to the first row of coupons being closest to the in-gate and consequently exhibiting the highest porosity. Conversely, the coupons in the fourth row, situated farthest from the in-gate, demonstrate the lowest porosity.

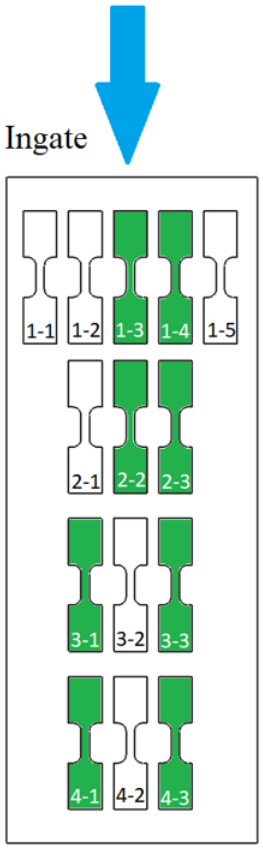

Figure 4.1: An illustration of the plate from which the coupons are extracted. The ones marked with green are the ones that were used in this report.

4.1 Simulation result

In this section, the simulation results for the material model and will be presented. It contains different results such as plasticity and failure simulation and calibration for different coupons.

4.1.1 Plastic hardening calibration

Figure 4.2 shows the results for the calibrated parameters for the linear and plastic hardening part of the material model. It is evident that the parameters effectively capture the material's hardening behavior.

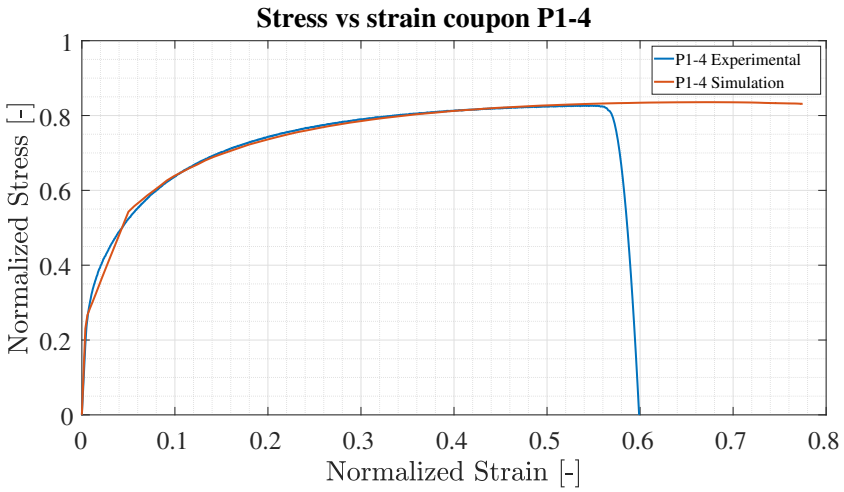

Figure 4.2: Coupon 1-4 stress-strain without damage criteria.

4.1.2 Damage calibration

Table 4.1 provides the optimized parameters and Figure 4.3 illustrates optimized failure curves. It is evident that the modified GISSMO failure curve requires a downward adjustment of about 34 % compared to the experimental failure curve.

Table 4.1: The normalized GISSMO parameters optimized for coupon 1-4.

Failure curve type	m	n	Normalized SF
Experimental failure curve	5	3	1
Modified failure curve	5	3	0.66

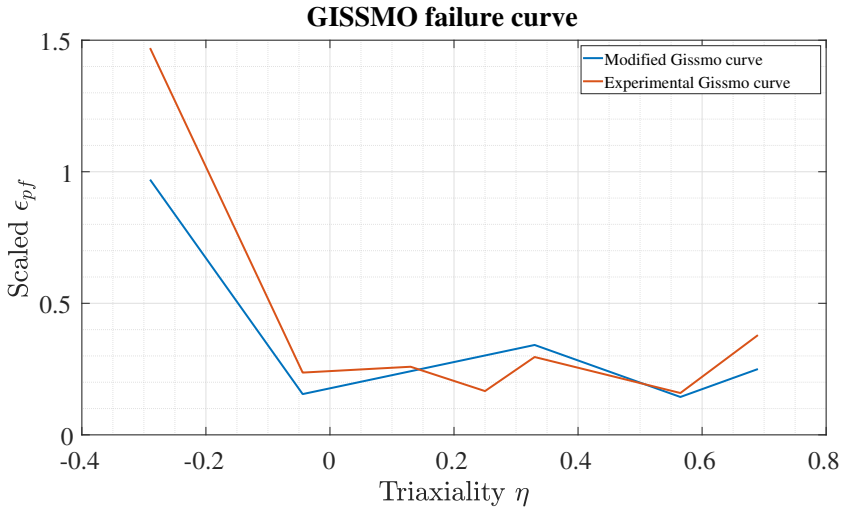

Figure 4.3: Optimized GISSMO failure curve for coupon 1-4.

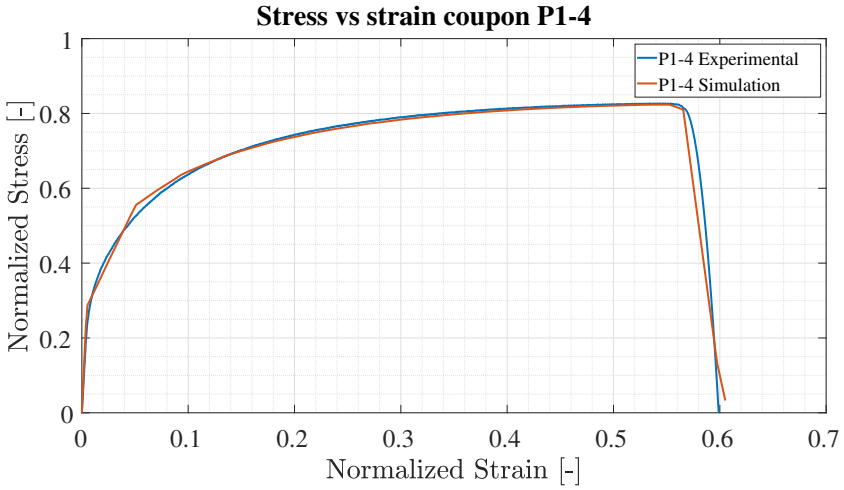

Figure 4.4: Coupon 1-4 stress-strain with damage criteria.

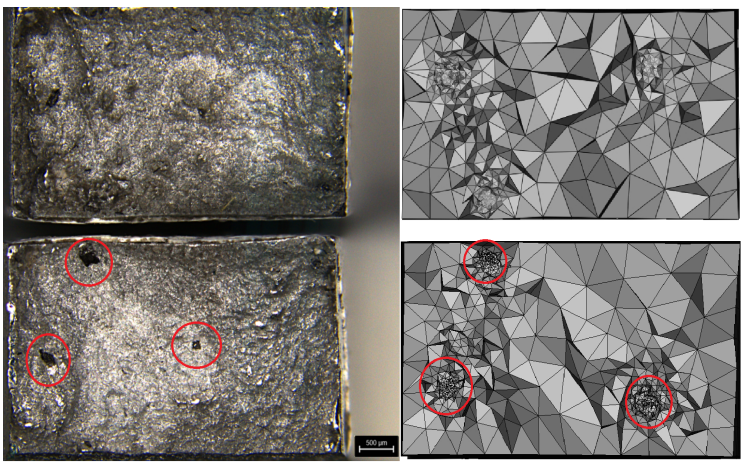

(a) Real coupon fracture surface.

(b) Simulation coupon fracture surface.

Figure 4.5: Comparison of fracture surface.

Figure 4.4 illustrates the comparison between experimental data and the optimized stress-strain curve for coupon 1-4 which align perfectly. Figure 4.5 displays the fracture surface from both mechanical tests and simulations. It is evident that the simulation accurately captures the fracture surface, closely resembling that of the real coupon.

In Figure 4.6, the result for when applying the optimized material model for coupon 1-4 on the other coupons is shown. The optimized material model predicts the failure of coupon 2-3 fairly well, while the prediction for coupon 1-3 is less accurate but still acceptable. However, the optimized material model fail to reflect the behavior of coupons 4-1 and 4-3.

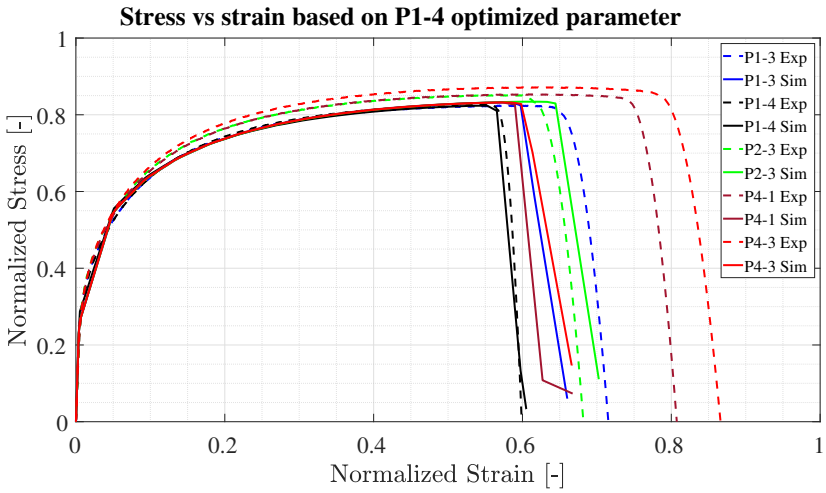

Figure 4.6: Stress-strain for different coupons based on optimized parameter of coupon 1-4.

As the other coupons are not captured with the optimized material model for coupon 1-4, identical optimization procedures are conducted for all coupons. The result for this is shown in Figure 4.7, and in Table 4.2 the value of the material parameters are shown.

Table 4.2: Material parameters, values are normalized with coupon 1-4 being used as the reference value, hence all its coefficients are equal to 1.

coupon number	A	B	C	H	SF
1-3	1	1.02	1.03	1.01	1.08
1-4	1	1	1	1	1
2-3	1	1	1.08	1.02	0.95
4-1	1	1	1.08	1.02	1.35
4-3	1.01	1.02	1.27	1.11	1.62

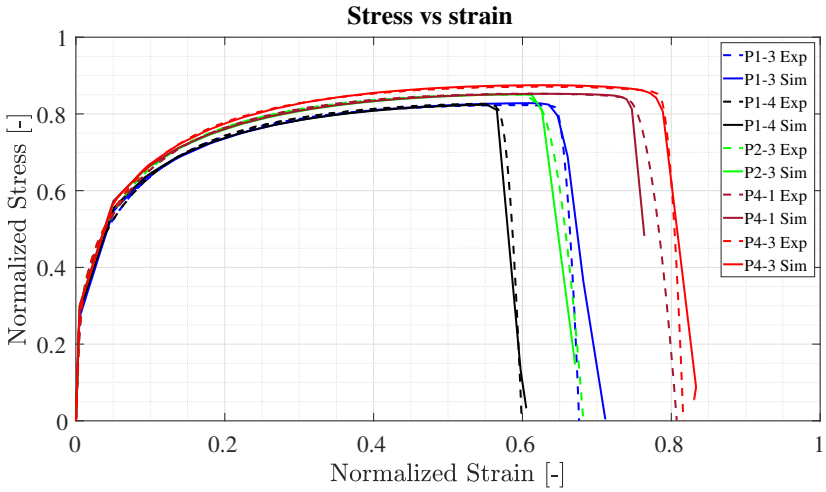

Figure 4.7: Stress - Strain for different coupons based on optimized parameter

4.2 Mesh regularization

Figure 4.8 and Table 4.3 illustrate the results of the mesh regularization study. It is apparent that for element sizes smaller than 0.1 mm, the failure response has converged. Additionally, the difference in failure strain between 0.5 mm and 0.025 mm is approximately 11 %.

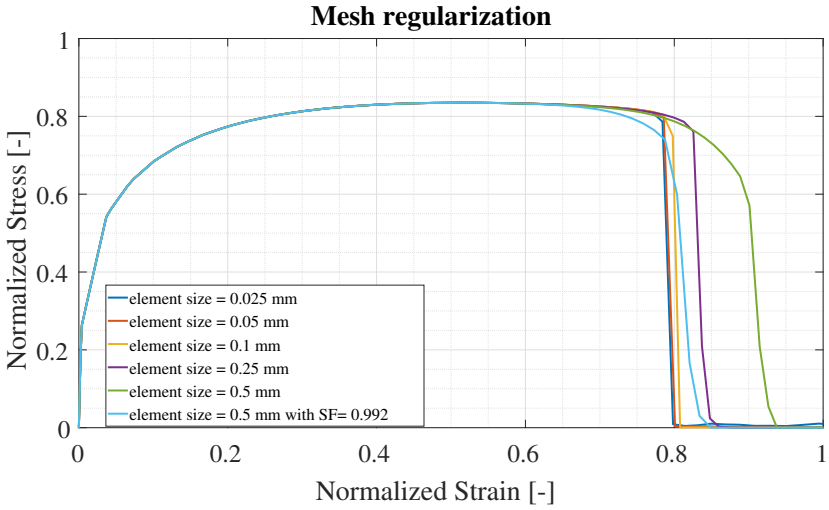

Figure 4.8: Result of the mesh regularization for smaller element sizes.

4.3 Investigating porosity-related factors

The disparity between the simulation and experimental data, as illustrated in Figure 4.6, can be attributed to various factors stemming from the presence of pores. To conduct a comprehensive investigation, different factors have been explored, and the results are explained as follows.

Table 4.3: Failure strain for different element size.

Element size [mm]	Normalized Strain [-]
0.025	0.7843
0.05	0.7857
0.1	0.7971
0.25	0.8257
0.5	0.8857

4.3.1 Non-porous conditions

As outlined in Chapter 3, various factors influence the material failure in the presence of porosity, including pore placement, size, volume, and stress triaxiality. Consequently, it is valuable to explore material behavior under pore-free conditions.

To accomplish this, the initial step involves calibrating all coupons with porosity for both plasticity and failure. Subsequently, the optimized parameters corresponding to each coupon are applied to simulate pore-free coupons, enabling the observation of material behavior in the absence of pores.

The stress-strain curves for these coupons are presented in Figure 4.9. Interestingly, contrary to real test data, coupon 2-3 breaks earlier than coupon 1-4.
Based on the findings derived from Figure 4.9, it is determined that the presence of pores significantly impacts the material's behavior. Consequently, the next phase of the study will focus on investigating various aspects of the pores, including their shape, size, and distribution.

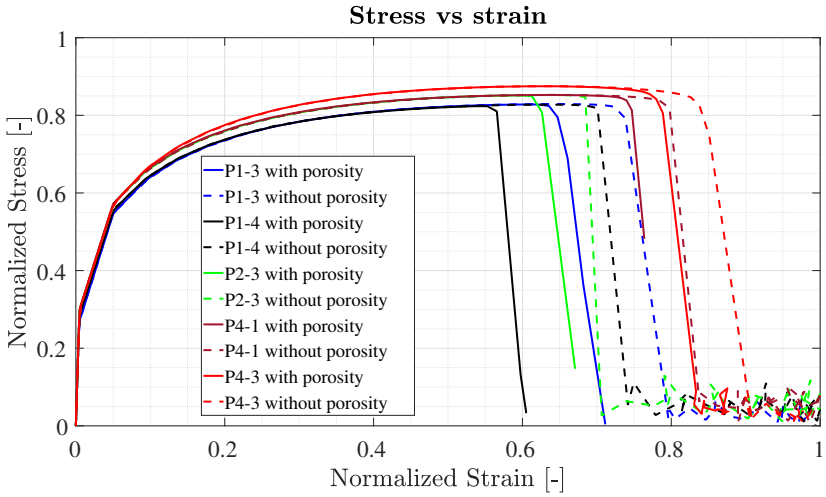

Figure 4.9: Comparison of stress-strain behavior in pore-free and porous coupons.

4.3.2 Porous conditions

This section presents results from various studies on different types of pore geometries. Initially, the impact of the location and shapes of simplified pores is discussed. Subsequently, the results regarding the influence of the pore volume fraction on the material's ductility is presented. Finally, findings related to the geometries of pores derived from CT scanned coupons is discussed.

4.3.2.1 Effect of pore shape on material behavior

The results from the pore geometry study, as depicted in Figure 4.10, indicate a significant impact of pore geometries on the failure of the material. The plasticity part of the different pore geometries is very similar, hence the graph only shows the failure part of the curves, where there is a difference.
Moreover, in Figure 4.11, the effect of the distance between pores is shown. However, one more parameter comes into play in this test, which is the distance between the pores and the boundaries, which affects the results. A more detailed result of the impact of the boundary is presented in section 4.3.2.2, which complements the results presented here.

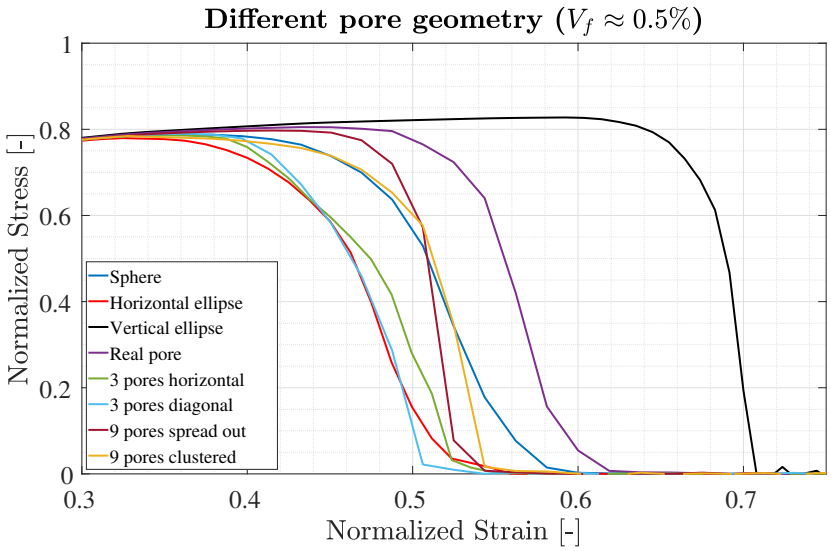

Figure 4.10: Comparison of stress-strain behavior for different pore geometry.

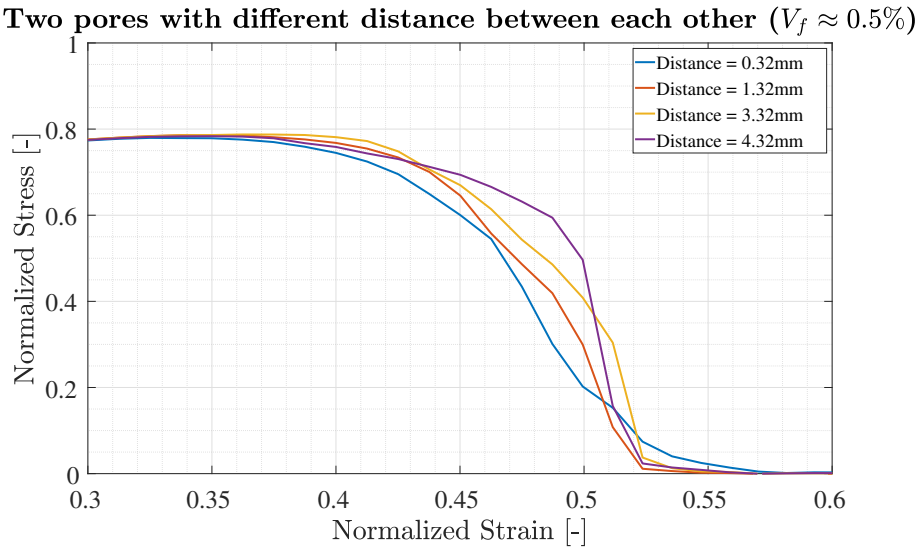

Figure 4.11: Comparison of different models containing two pores.

4.3.2.2 Effect of Pore size and boundary on material behavior

Figure 4.12 shows the effect the pore size on the failure strain. Moreover, the results regarding the impact of the boundary can be seen in Figure 4.13, where the label shows the smallest distance from the pore to a boundary.

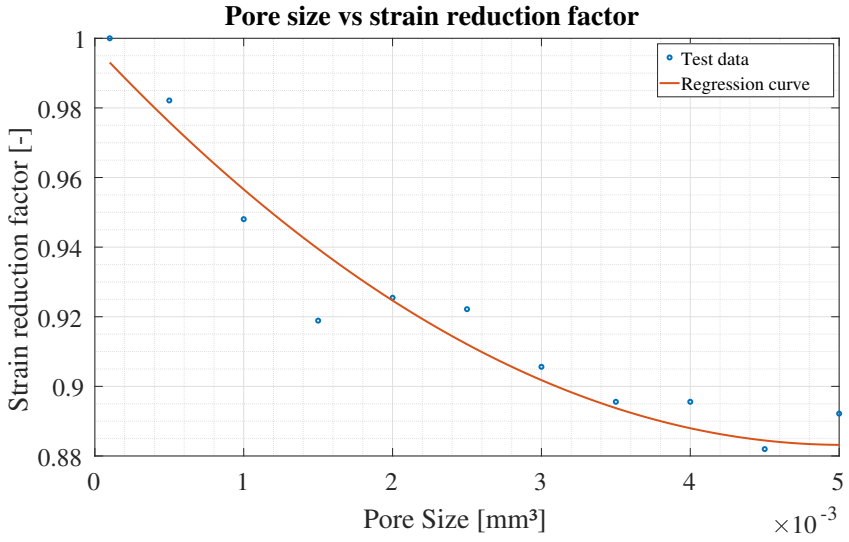

Figure 4.12: Impact of pore size on failure strain.

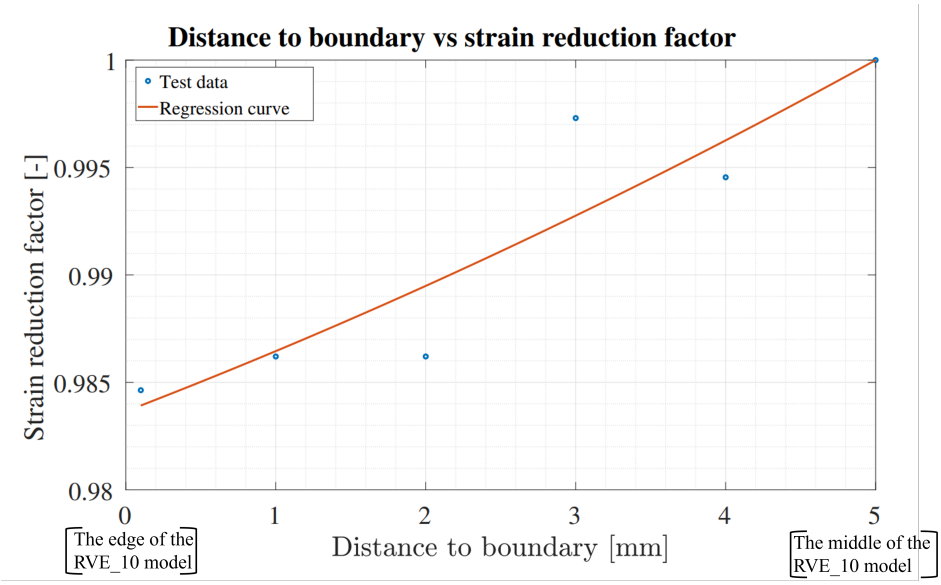

Figure 4.13: Impact of distance from boundary on failure strain.

4.3.2.3 Effect of pore radius on ductility

In Figure 4.14a, the difference in failure behaviour between a lower ϵ_{crit} value and a higher ϵ_{crit} value for different pore sizes is shown. Moreover, in Figure 4.14b the tensile ductility is shown. The tensile ductility is defined as the failure strain, ϵ_f, subtracted by the critical strain (where critical damage initiates), ϵ_{crit}.

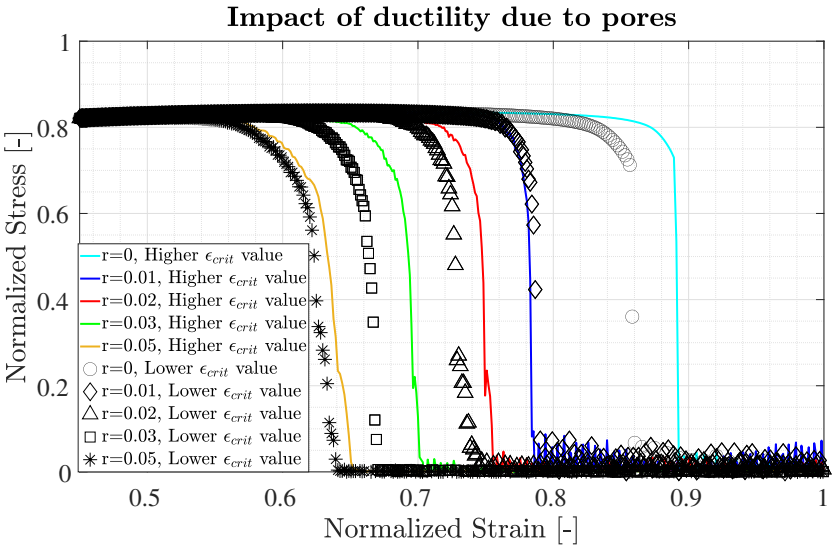

(a) Failure shape of the two different ϵ_{crit} values.

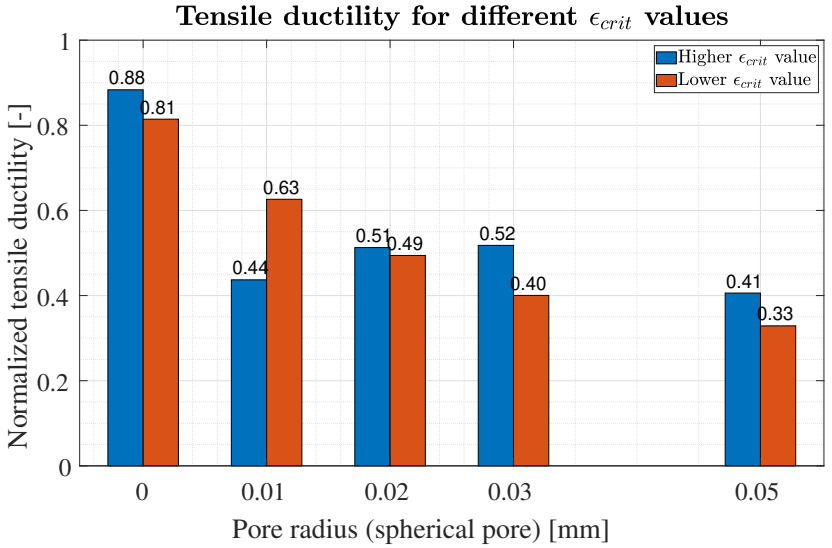

(b) The tensile ductility for the different values on ϵ_{crit}.

Figure 4.14: Impact of pores on a materials ductility.

4.3.3 Porosity-related factors on real coupon

In Figures 4.15 and 4.16, the relationship between the experimental failure strain and maximum pore size as well as the relationship between the experimental failure strain and the shortest distance to a boundary, are shown. Figure 4.15 illustrates that as pore size increases, failure strain decreases. Consequently, coupon 1-4, with the largest pore, exhibits the lowest failure strain, while coupon 4-3 demonstrates the highest failure strain. Notably, although coupon 3-1 and 2-3 possess the smallest pore size, smaller than coupon 4-3, they fail earlier.

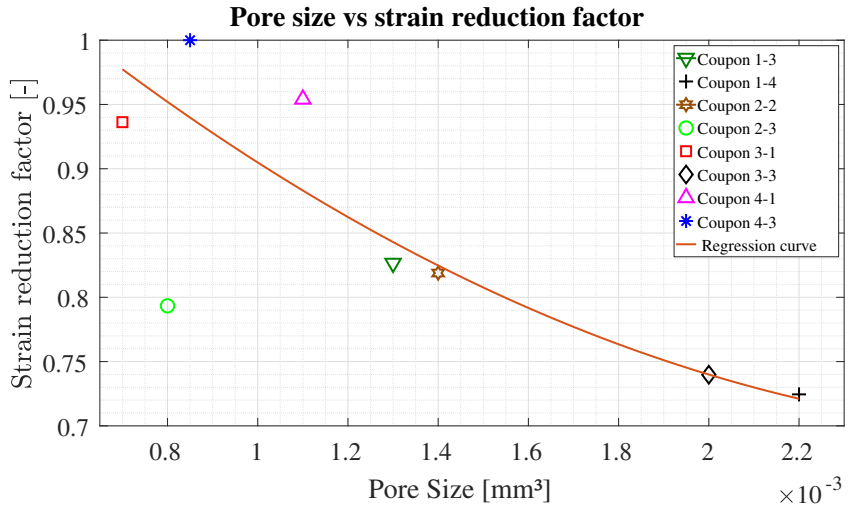

Figure 4.15: Impact of pore size on failure strain for coupons.

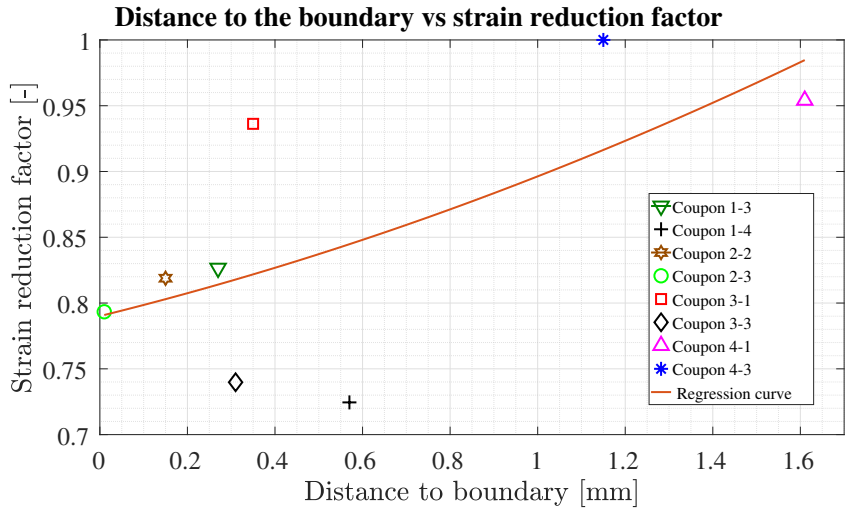

Figure 4.16: Impact of distance from boundary on failure strain for coupons.

As depicted in Figure 4.16, the further the pores are from the edge, the higher the failure strain is. Coupons 3-1 and 2-3, characterized by the smallest pore size, fail sooner due to the proximity of the pores to the boundary, in contrast to coupons 4-3 or 4-1.

Figure 4.17 shows the evolution of porosity and the propagation of cracks from the inception of the simulation until failure at three distinct time steps. This visualization illustrates the evolution of pores, the propagation of cracks through the coupon, their interaction with other pores, and their eventual contribution to fracture.

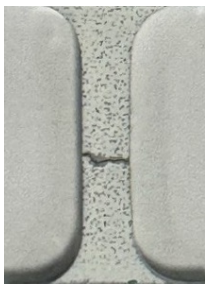

(a) The crack path from mechanical test.

(b) Coupon P1-3 crack growth.

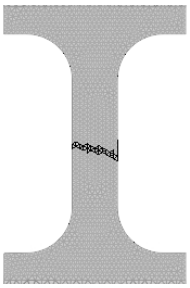

(c) The crack path from simulation.

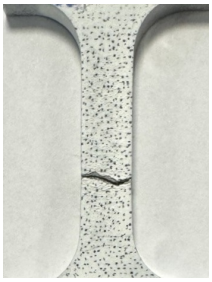

(d) The crack path from mechanical test

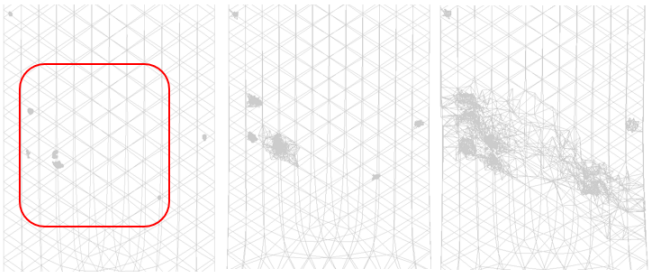

(e) Coupon P1-4 crack growth.

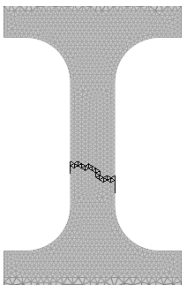

(f) The crack path from simulation.

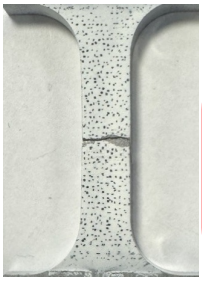

(g) The crack path from mechanical test

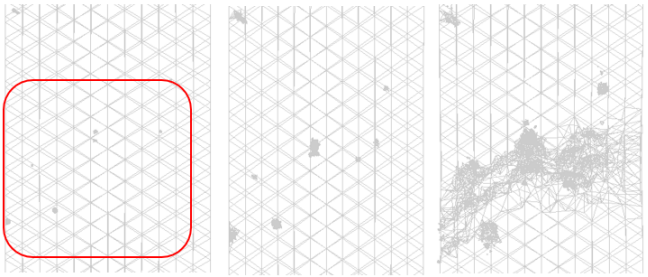

(h) Coupon P2-3 crack growth.

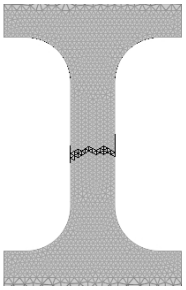

(i) The crack path from simulation.

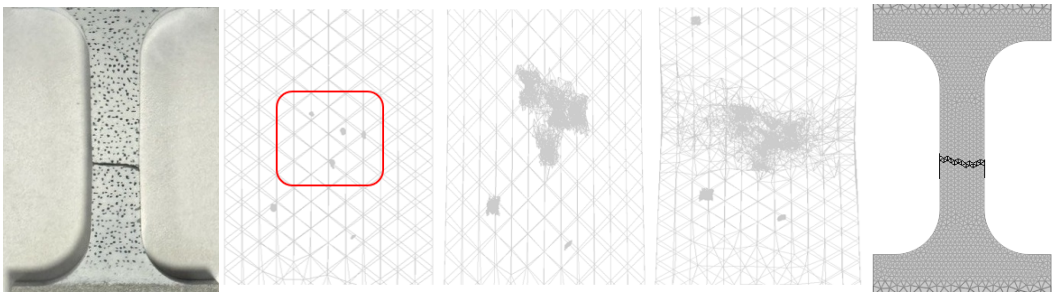

(j) The crack path from mechanical test

(k) Coupon P4-1 crack growth.

(l) The crack path from simulation.

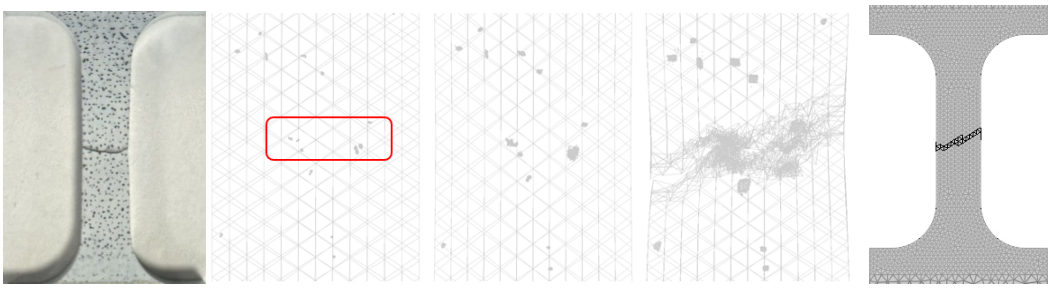

(m) The crack path from mechanical test

(n) Coupon P4-3 crack growth.

(o) The crack path from simulation.

Figure 4.17: Crack propagation due to porosity.

4.3.4 Calibration across all coupons

As seen in Table 4.2, the material constants for the different material models are very similar, however it is the scale factor of the failure curve that show significant differences. Because of this, it is not possible to generate one material model that captures all coupons, instead two material models are created. The material parameters for these models are shown in Tables 4.4 and 4.5. The first set, designated as group A, is tailored for coupons located close to the in-gate, suitable for those in the first and second rows of the prototype. The second set, referred to as group B, is intended for coupons situated farther from the in-gate, such as those in the third and fourth rows of the prototype.

Table 4.4: Material parameters for group A, normalized against the values from coupon 1-4.

A	B	C	H	m	n	ϵ_{crit}	SF
0.9971	0.9731	0.9990	1.0271	5	3	1.07	1.026

Table 4.5: Material parameters for group B, normalized against the values from coupon 1-4.

A	B	C	H	m	n	ϵ_{crit}	SF
1.0218	0.9996	1.1349	1.1031	5	3	1.03	1.41

In Figure 4.18 the result for when simulating all coupons with the material models group A and B is shown together with the experimental data. It is evident that the material parameters set of group A effectively captures the behavior of coupons 1-3, 1-4, 2-3, and 3-3, and with a reasonable approximation for coupon 2-2. Conversely, the material parameters for group B adequately predicts the behavior of coupon 3-1, 4-1 and 4-3.

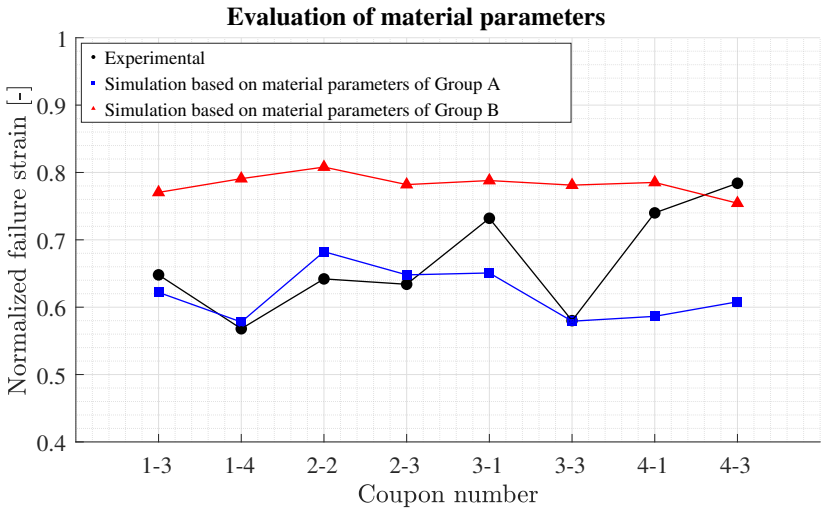

Figure 4.18: Failure strain for all coupons based on material parameters of groups A and B

5

Discussions

5.1 Damage Calibration

Table 4.1 and Figure 4.3 display the calibrated parameters and failure curve for both the modified and experimental failure curves. The significant difference in adjustment stems from the optimized modified failure curve used in this study, in contrast to the experimental failure curve, which was based on raw, unprocessed data. Theoretically, the stress triaxiality for a tensile test is assumed to be around 0.33. Thus, the data for the uni-axial tensile test was adjusted to reflect a triaxiality of 0.33.

However, during the simulation, tracking the stress triaxiality in critical elements revealed that this variable deviates when damage couples with plasticity. In the initial experimental failure data, the plastic failure strain for stress triaxiality ranges of 0.18 to 0.25 and 0.4 to 0.56 are considerably lower than the failure strain at a stress triaxiality of 0.33. This requires a substantial upward adjustment.

This occurrence prompted further investigation into the effect of the failure curve shape. Consequently, another failure curve was added to assess its impact. A new failure curve was created based on the experimental one, with the assumption that all stress triaxialities between -0.044 and 0.565 have the same plastic failure strain. The optimization was also conducted based on this failure curve and the result is shown in Table 5.1 and Figure 5.1.

Table 5.1: Coupon 1-4 GISSMO failure curve parameters.

Failure curve type	m	n	Normalized SF
Experimental failure curve	5	3	1
Flat failure curve	5	3	0.97

By comparing the results, it was concluded that most of the critical elements exhibited a stress triaxiality between 0.4 and 0.56 at failure, although other triaxiality states were also present. Moreover, it could be concluded that since most of the failures occur within a triaxiality range of 0.25 to 0.56, the shape of the failure curve does not significantly affect the results as long as the deviation from a straight line is minimal for the case of a uniaxial test and in the presence of pores.

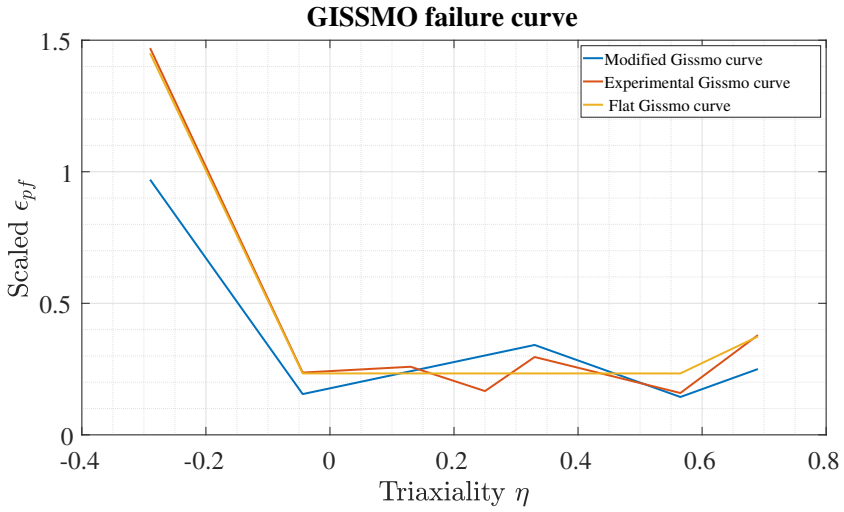

Figure 5.1: Optimized GISSMO failure curve for coupon 1-4

5.2 Investigating porosity-related factors

5.2.1 Non-porous conditions

As illustrated in Figure 4.9, coupon 2-3 breaks earlier than coupon 1-4 in non-porous condition. This discrepancy arises because, without any porosity, the stress triaxiality of all coupons have similar trend at critical element, as shown in Figure 5.2. Consequently, coupon 2-3, which has the lowest failure curve as shown in Figure 5.3, exhibiting the most brittle failure curve, breaks earlier. Based on this result and observations from the simulation, it is concluded that stress triaxiality varies depending on the presence or absence of porosity, as well as differing among different coupons. Although, it was shown in the previous chapter that, the other factor such as size and location of the pores have significant effects the stress triaxiality and also failure strain.

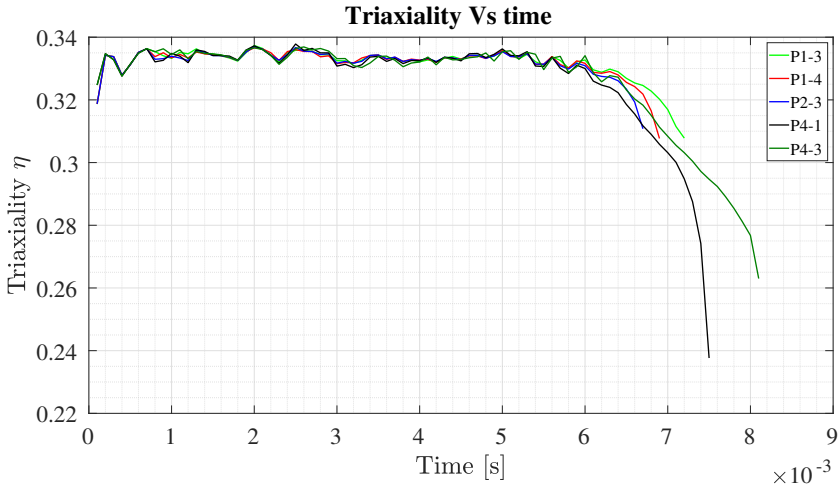

Figure 5.2: Stress triaxiality vs time for different coupons.

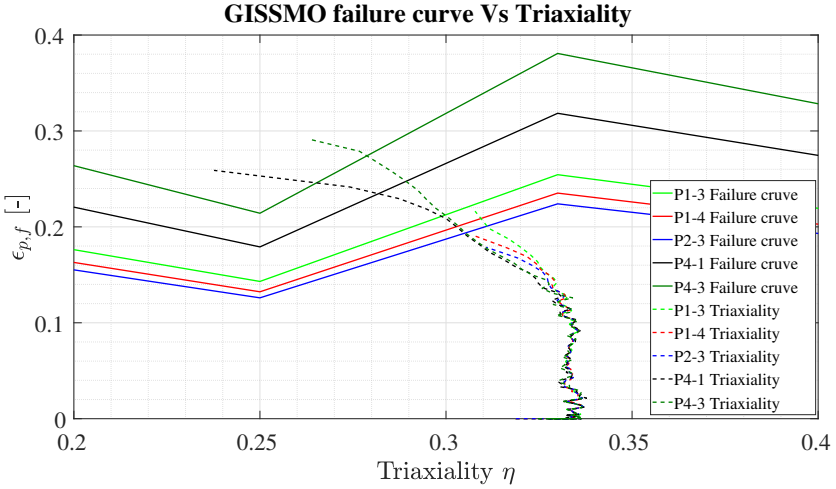

Figure 5.3: GISSMO failure curve for different coupons.

5.2.2 Porous conditions

The examination of the results presented in Figure 4.10 reveals that an optimal scenario involves a pore elongated parallel to the load direction, while the least favorable scenario occurs when the pore is elongated perpendicular to the load at 90°. This marked contrast underscores the substantial influence of pore shape and orientation, although such idealized pore configurations are rarely encountered. Typically, a mixture of orientations is found, as evidenced by the intermediate failure strain of the actual pore from the CT-scan, situated between the horizontal and vertical ellipses.

Further analysis of Figure 4.10 highlights the effect of numerous smaller pores on the material strength. It is evident that a multitude of small pores contributes to a higher failure strain compared to a few larger ones, with the nine-pore models outperforming the spherical ones. It is also apparent that dispersing the pores rather

than clustering them is advantageous, as it reduces the likelihood of pore coalescence into a larger defect. This is demonstrated by the nine-pore model clustered at the center, which exhibits a failure strain similar to that of a single spherical pore model. Given the consistent volume fraction across these models, it can be inferred that the practice of merging adjacent pores [9] into a single entity is a valid approximation for accurate results.

While the relative positioning of pores is important, the critical factor is the distance between them rather than their arrangement. For instance, models with three horizontal pores and three diagonal pores show negligible differences in failure when the inter-pore distance is identical, despite varied placements. Conversely, Figure 4.11 presents an opposite scenario where two horizontally aligned pores vary in separation distance. As anticipated, and in line with the nine-pore model, increasing the inter-pore distance enhances failure strength. However, an additional factor emerges: the proximity of the pore to the boundary. The greatest separation (4.32 mm) results in a lower failure strength compared to distances of 1.32 and 3.32 mm, indicating that the boundary's proximity exerts a more pronounced effect than the inter-pore spacing.
The significance of boundary proximity is further discussed in section 5.2.4.

5.2.3 Ductility with pores

The effect of the ϵ_{crit} is such that a lower value leads to earlier onset of critical damage while a higher value leads to later onset of critical damage. The failure should not be affected by the onset of critical damage, instead it should always fail at the given failure strain. Therefore, it would result in that a lower ϵ_{crit} value results in higher ductility and vice versa. In contrast, the results seen in Figures 4.14a and 4.14b show that for nearly all pore volumes, a reduced failure strain is recorded, and a lower ϵ_{crit} correlates with decreased ductility.

This phenomenon might be attributed to the characteristics of the GISSMO curve. A decrease in the ϵ_{crit} implies an earlier initiation of critical damage, which can be seen in eq.(2.7) where a smaller ϵ_{crit} gives a higher F meaning the instability/-critical damage point is reached faster. This earlier initiation of critical damage is potentially causing an earlier and more significant shift in triaxiality, as depicted in Figure 5.3. This shift results in the curve being intersected at a different point. Given that the GISSMO curve is not linear, a new failure strain emerges, which can be either greater or lesser, hence the variation in results and the non-uniformity of the failure strain. Consequently, ductility varies, and a higher ϵ_{crit} could potentially result in greater ductility.

In light of these findings, the coupons were also scrutinized to determine if the ϵ_{crit} influenced their outcomes. As evidenced in Figures 5.4a and 5.4b, there is an effect, albeit significantly less pronounced than in the RVE, to the extent that it can be disregarded. This is deduced from the near-perfect congruence of the curves in Figure 5.4a, suggesting the ϵ_{crit} has minimal impact on these models.

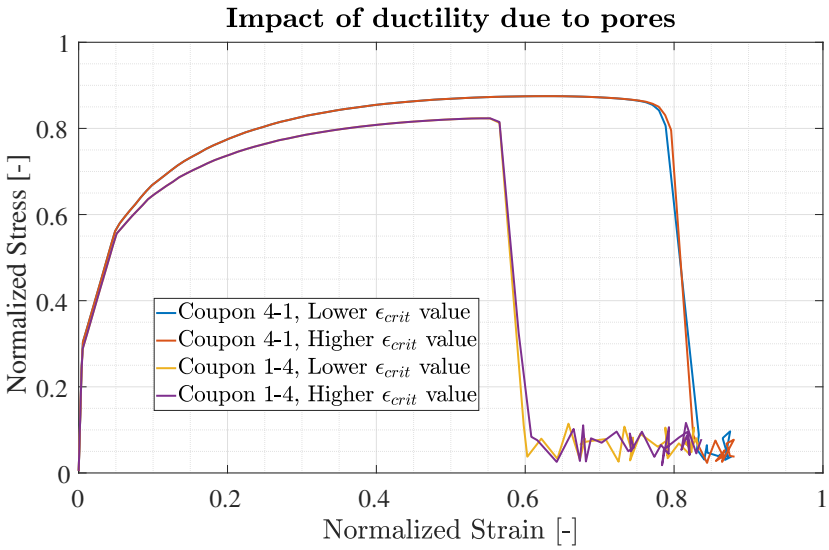

(a) Failure shape of the two different ϵ_{crit} values.

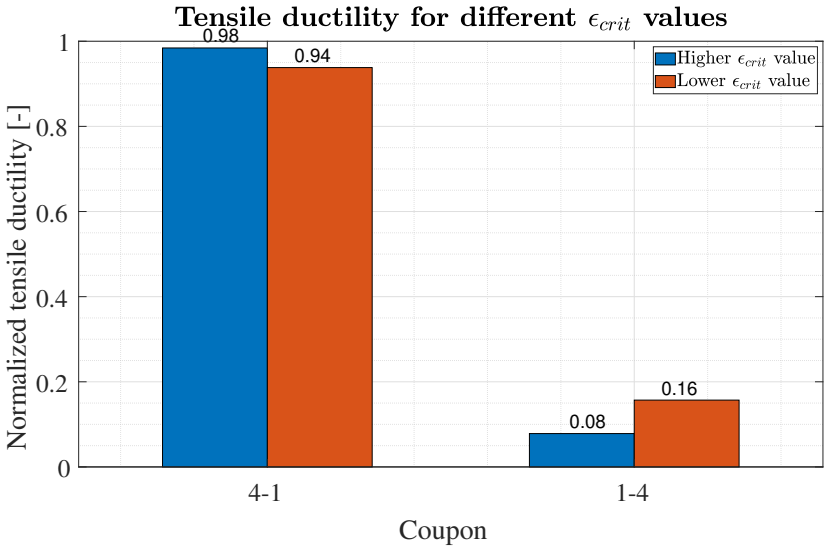

(b) The tensile ductility for the different values on ϵ_{crit}.

Figure 5.4: Results showing the impact the pores have on a materials ductility.

Despite these findings, the outcomes are considered trustworthy, as the behavior of ductility is consistent with anticipated trends: a higher volume of porosity results in a reduced failure strain. This behavior is in agreement with previously conducted research and the tendencies that have been documented [6].

5.2.4 The effect of pore size and distance to the boundary

Building upon the insights from the preceding section, a thorough investigation into the boundary's influence reveals that the proximity to the boundary significantly affects the material's strength, as depicted in Figure 4.13. This pattern is mirrored

in the coupon tests, illustrated in Figure 4.16, where the failure strain exhibits a roughly linear relationship with the boundary distance.

Examining the role of pore size, Figure 4.12 demonstrates that the failure strain varies exponentially with pore size. Initially, the introduction of porosity leads to a sharp decline in failure strain, but the rate of change diminishes as the porosity increases. This behavior is consistent with other research findings that have observed a similar trend in the curve [8], [7]. The coupon comparisons, as shown in Figure 4.15, suggest a more linear variation, a discrepancy that may stem from limited data and the varying distances of the pores to the boundary. Notably, coupon 2-3, with the smallest pore size yet nearest to the boundary, exhibits a significantly low failure strain.

This raises the question of whether pore size or proximity to the boundary has a greater impact. The coupon data, presented in Figures 4.15 and 4.16, suggests that the influence of boundary distance becomes more pronounced with smaller pore sizes. This is inferred from comparing coupons 4-3 and 2-3, which, despite similar pore sizes, show a pronounced contrast in failure strain due to the differing boundary proximities. A comparison between coupons 2-3 and 2-2 reveals comparable failure strains, despite a significant difference in pore size, underscoring the boundary distance's effect.
In a simplified scenario with a single pore, as discussed in Section 4.3.2.2, identifying a pattern becomes more feasible. Data encompassing various pore sizes and boundary distances are plotted in Figure 5.5. It is apparent that the failure strain's rate of change in relation to pore size remains relatively constant, while the effect of boundary proximity is such that the closer the pore is to the boundary, the lower the failure strain appears on the graph.

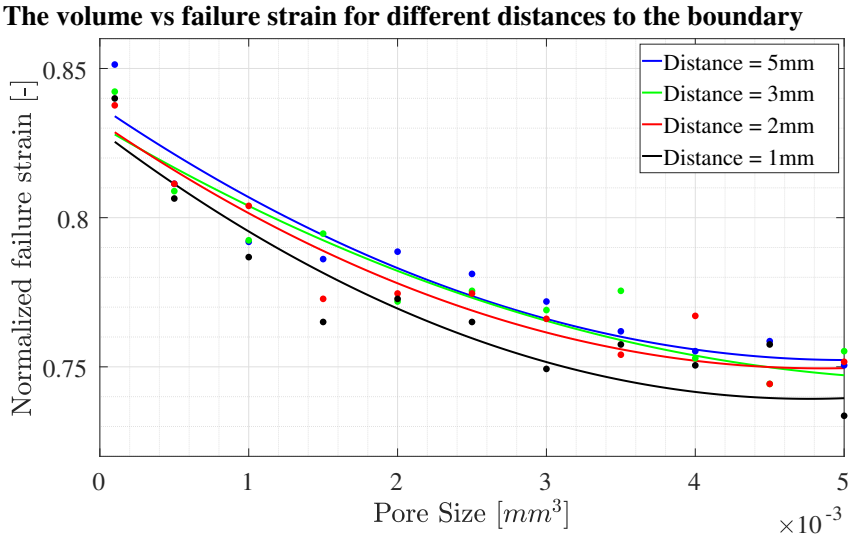

Figure 5.5: The effect of the pore size and distance to the boundary on the failure strain.

The data also suggests that the boundary's influence is more significant for larger pore sizes, as indicated by the greater disparity between lines for larger pores compared to smaller ones.

These observations lead to the conclusion that the material model effectively captures the trends and behaviors associated with pore inclusion. However, only the behaviour of a single pore has been studied and including multiple may lead to inconsistent results.

5.3 Calibration across all specimens

Figure 4.18 displays stress-strain comparisons between experimental and simulation data, utilizing the optimized parameters from Tables 4.4 and 4.5 respectively. Tables 5.2 and 5.3 present the maximum relative error between the experimental and simulation data for both material sets.

This highlights the necessity of having two material models. The model for group A accurately captures the behavior of coupons 1-3, 1-4, 2-2, 2-3 and 3-3 as evidenced by the relative error of approximately 6 %, which is acceptable. Conversely, for coupon 4-1 and 4-3 a maximum relative error are about 20 % 22 %,respectively, indicating a significant discrepancy.

The opposite behavior is observed when using the material model related to group B; the mentioned coupons exhibit a high relative error, with a maximum of 39 %, while coupons 3-3, 4-1 and 4-3 show a lower error, with a maximum of 7 %.

It should be noted that the error may also be attributed to various factors in the modeling process, such as CT scanning, porosity extraction, cleaning procedures or material characteristics that are not accounted for in the model. In conclusion, it can be observed that two sets of parameters are reasonably effective in predicting the material's behavior.

Table 5.2: Comparison of failure strain between experimental and simulation based on material parameters of group A

Coupon number	$\epsilon_{f,exp}$	$\epsilon_{f,sim}$	Relative error
1-3	0.648	0.622	4 %
1-4	0.578	0.568	1.73 %
2-2	0.642	0.682	6.23 %
2-3	0.634	0.648	2.2 %
3-1	0.732	0.651	11.9 %
3-3	0.58	0.579	0.14 %
4-1	0.74	0.586	20.76 %
4-3	0.784	0.608	22.45 %

Table 5.3: Comparison of failure strain between experimental and simulation based on material parameters of group B

Coupon number	$\epsilon_{f,exp}$	$\epsilon_{f,sim}$	Relative error
1-3	0.648	0.770	18.89 %
1-4	0.578	0.791	39.23 %
2-2	0.642	0.808	25.86 %
2-3	0.634	0.782	23.34 %
3-1	0.732	0.788	7.65 %
3-3	0.58	0.781	25.76 %
4-1	0.74	0.785	6.11 %
4-3	0.784	0.755	3.65 %

5.4 Mesh regularization

In finite element analysis, it is expected that larger element sizes result in larger failure strain, as demonstrated by the findings depicted in Figure 4.8 and summarized in Table 4.3. It is observed that convergence occurred for element sizes smaller than 0.1 mm. Additionally, the difference in failure strain between element sizes of 0.5 mm and 0.025 mm is approximately 11 %. However, if the aim is for the element size of 0.5 mm to exhibit the same failure strain as the 0.025 mm one, the failure curve would need to be multiplied by a factor of 0.992, which is roughly equal to 1. Consequently, it can be assumed that for this range of element sizes, mesh regularization is not necessary.

5.5 General discussion

The transition from a CT-scanned image to a finite element model encountered several challenges. The software RETOMO was employed to generate a mesh, which presented the primary issue. The CT-scanned images lacked orientation with respect to any plane, as illustrated in Figure A.1. Consequently, manual orientation was required to align the images with the modeled coupon, potentially introducing placement errors. Additionally, certain pores needed to be cleaned to prevent error messages during LS-DYNA simulations. This cleaning process involved either remeshing the pores in ANSA, which could slightly alter their shape, or removing/deleting elements with complex geometries or those inadequately captured in the CT scans. These steps introduced potential sources of error, suggesting that some results could be enhanced by refining this process. Nevertheless, the failure surface and the location of the failure were accurately captured for all coupons, indicating that the results remain reliable.

6
Conclusions and future work

The goal of this report was to predict the behavior of pores in aluminum using a virtual model and apply a homogenized material model capable of capturing all types of porosity. A virtual model that achieved results comparable to test outcomes was successfully created, with reproduced results being nearly identical in terms of stress-strain curves and failure surfaces. However, it was not possible to develop a material model that could capture all coupons with varying porosity levels. Despite this, the behavior of the pores was successfully captured, indicating that creating a homogenized model is within reach.

Since it is possible to generate a virtual model that captures the failure with pores, the next step is homogenization. The most important aspect is to determine all the variables and factors that impact the material model and then implement them. In this project, it was discovered that pore size and distance can be quite similar, but the failure strain can vary significantly, making it challenging to capture all coupons.

Some errors could be due to the failure model, specifically the GISSMO curve. The only loading case for which there was a CT-scanned coupon was uniaxial tension, and the other loading cases were based on old tests done on cast aluminum, where the porosity content was unknown. Therefore, an improvement would be to reproduce the GISSMO curve with different loading scenarios, as shown in Figure 2.6, using coupons with known porosity content. This would eliminate some errors and thereby provide more accurate results.

Bibliography

[1] W. Kowalczyk, R. Dańko, M. Górny, M. Kawalec, and A. Burbelko, "Influence of high-pressure die casting parameters on the cooling rate and the structure of en-ac 46000 alloy," *Materials*, vol. 15, no. 16, 2022, ISSN: 1996-1944. DOI: 10.3390/ma15165702. [Online]. Available: https://www.mdpi.com/1996-1944/15/16/5702.

[2] S. L. dos Santos, R. A. Antunes, and S. F. Santos, "Influence of injection temperature and pressure on the microstructure, mechanical and corrosion properties of a alsicu alloy processed by hpdc," *Materials & Design*, vol. 88, pp. 1071–1081, 2015, ISSN: 0264-1275. DOI: https://doi.org/10.1016/j.matdes.2015.09.095. [Online]. Available: https://www.sciencedirect.com/science/article/pii/S0264127515305049.

[3] M. Iversen and A. Årmann, *Characterisation of natural fibre composites using x-ray computer tomography aided engineering*, 2023.

[4] Y. Zhang, F. Shen, J. Zheng, *et al.*, "Ductility prediction of hpdc aluminum alloy using a probabilistic ductile fracture model," *Theoretical and Applied Fracture Mechanics*, vol. 119, p. 103 381, 2022, ISSN: 0167-8442. DOI: https://doi.org/10.1016/j.tafmec.2022.103381. [Online]. Available: https://www.sciencedirect.com/science/article/pii/S016784422200129X.

[5] K. Choi, E. Barker, G. Cheng, and X. e. a. Sun, "Predicting stress vs. strain behaviors of thin-walled high pressure die cast magnesium alloy with actual pore distribution," *SAE Int. J. Mater. Manf*, 2016. DOI: https://doi.org/10.4271/2016-01-0290.

[6] E. Lordan, Y. Zhang, K. Dou, *et al.*, "On the probabilistic nature of high-pressure die casting," *Materials Science and Engineering: A*, vol. 817, p. 141 391, 2021, ISSN: 0921-5093. DOI: https://doi.org/10.1016/j.msea.2021.141391. [Online]. Available: https://www.sciencedirect.com/science/article/pii/S0921509321006602.

[7] E. Lordan, J. Lazaro-Nebreda, Y. Zhang, K. Dou, P. Blake, and Z. Fan, "On the relationship between internal porosity and the tensile ductility of aluminium alloy die-castings," *Materials Science and Engineering: A*, vol. 778, p. 139 107, 2020, ISSN: 0921-5093. DOI: https://doi.org/10.1016/j.msea.2020.139107. [Online]. Available: https://www.sciencedirect.com/science/article/pii/S0921509320301957.

[8] C. Cáceres and B. Selling, "Casting defects and the tensile properties of an al-simg alloy," *Materials Science and Engineering: A*, vol. 220, no. 1, pp. 109–116, 1996, ISSN: 0921-5093. DOI: https://doi.org/10.1016/S0921-5093(96)

10433-0. [Online]. Available: https://www.sciencedirect.com/science/article/pii/S0921509396104330.

[9] S. Streck, T. Wiege, S. Dietrich, R. Herger, and V. Schulze, "Influence of pores on the lifetime of die cast aluminium alloys studied by fracture mechanics and x-ray computed tomography," *Engineering Fracture Mechanics*, vol. 284, p. 109 243, 2023, ISSN: 0013-7944. DOI: https://doi.org/10.1016/j.engfracmech.2023.109243. [Online]. Available: https://www.sciencedirect.com/science/article/pii/S0013794423002011.

[10] ItalPresseGauss, *What is high pressure die casting - hpdc*. [Online]. Available: https://www.italpressegauss.com/my-application-and-industry/application-by-process/what-is-high-pressure-die-casting.

[11] M. Jolly and L. Katgerman, "Modelling of defects in aluminium cast products," *Progress in Materials Science*, vol. 123, p. 100 824, 2022, A Festschrift in Honor of Brian Cantor, ISSN: 0079-6425. DOI: https://doi.org/10.1016/j.pmatsci.2021.100824. [Online]. Available: https://www.sciencedirect.com/science/article/pii/S0079642521000487.

[12] V. Khalajzadeh, K. Carlson, and D. e. a. Backman, "A pore-centric model for combined shrinkage and gas porosity in alloy solidification," *Metallurgical and Materials Transactions A*, vol. 48, 2017.

[13] R. M. Auenhammer, L. P. Mikkelsen, L. E. Asp, and B. J. Blinzler, "Automated x-ray computer tomography segmentation method for finite element analysis of non-crimp fabric reinforced composites," *Composite Structures*, vol. 256, p. 113 136, 2021, ISSN: 0263-8223. DOI: https://doi.org/10.1016/j.compstruct.2020.113136. [Online]. Available: https://www.sciencedirect.com/science/article/pii/S0263822320330622.

[14] A. Marion, *Introduction to Image Processing*. Springer New York, NY, 1991. DOI: https://doi.org/10.1007/978-1-4899-3186-3.

[15] L. S. T. (LST), *Ls-dyna keyword user's manual volume ii material models*. [Online]. Available: https://www.dynasupport.com/manuals/ls-dyna-manuals/ls-dyna_manual_volume_ii_r13.pdf.

[16] N. S. Ottosen and M. Ristinmaa, "9 - introduction to plasticity theory," in *The Mechanics of Constitutive Modeling*, N. S. Ottosen and M. Ristinmaa, Eds., Oxford: Elsevier Science Ltd, 2005, pp. 203–246, ISBN: 978-0-08-044606-6. DOI: https://doi.org/10.1016/B978-008044606-6/50009-6. [Online]. Available: https://www.sciencedirect.com/science/article/pii/B9780080446066500096.

[17] E. Doege and T. Hallfeld, "Metal working: Stretching of sheets," in *Encyclopedia of Materials: Science and Technology*, K. J. Buschow, R. W. Cahn, M. C. Flemings, *et al.*, Eds., Oxford: Elsevier, 2001, pp. 5518–5521, ISBN: 978-0-08-043152-9. DOI: https://doi.org/10.1016/B0-08-043152-6/00964-5. [Online]. Available: https://www.sciencedirect.com/science/article/pii/B0080431526009645.

[18] A. Haufe, P. Dubois, F. Neukamm, and M. Feucht, "Gissmo – material modeling with a sophisticated failure criteria," 2011. DOI: 10.13140/RG.2.2.27677.92646.

[19] P.-O. Bouchard, L. Bourgeon, S. Fayolle, and K. Mocellin, "An enhanced lemaitre model formulation for materials processing damage computation," *International Journal of Material Forming*, vol. 4, pp. 299–315, Sep. 2010. DOI: 10.1007/s12289-010-0996-5.

[20] J. Effelsberg, A. Haufe, M. Feucht, F. Neukamm, and P. Dubois, "On parameter identification for the gissmo damage model," Jun. 2012.

[21] Z. Zhang, Y. Cui, and G. Yu, "Damaged and failure characterization of 7075-t6 al alloy based on gissmo model," *Journal of Mechanical Science and Technology*, vol. 35, Feb. 2021. DOI: 10.1007/s12206-021-0234-8.

[22] Y. Ge, L. Dong, H. Song, L. Gao, and R. Xiao, "On the prediction of material fracture for thin-walled cast alloys using gissmo," *Metals*, vol. 12, p. 1850, Oct. 2022. DOI: 10.3390/met12111850.

[23] A. R. Itani, *Modelling and evaluation of the methods for compression testing of thermoplastics*, 2021.

[24] K. Witowski, M. Feucht, and N. Stander, "An effective curve matching metric for parameter identification using partial mapping." [Online]. Available: https://www.dynalook.com/conferences/8th-european-ls-dyna-conference/session-4/Session4_Paper2.pdf.

[25] H. D. H Hooputra H Gese and H. Werner, "A comprehensive failure model for crashworthiness simulation of aluminium extrusions," *International Journal of Crashworthiness*, vol. 9, no. 5, pp. 449–464, 2004. DOI: 10.1533/ijcr.2004.0289. eprint: https://doi.org/10.1533/ijcr.2004.0289. [Online]. Available: https://doi.org/10.1533/ijcr.2004.0289.

A

Appendix 1

A.1 Orientation of coupons from CT scan

Figure A.1, shows the orientation of the coupon when imported from RETOMO to ANSA.

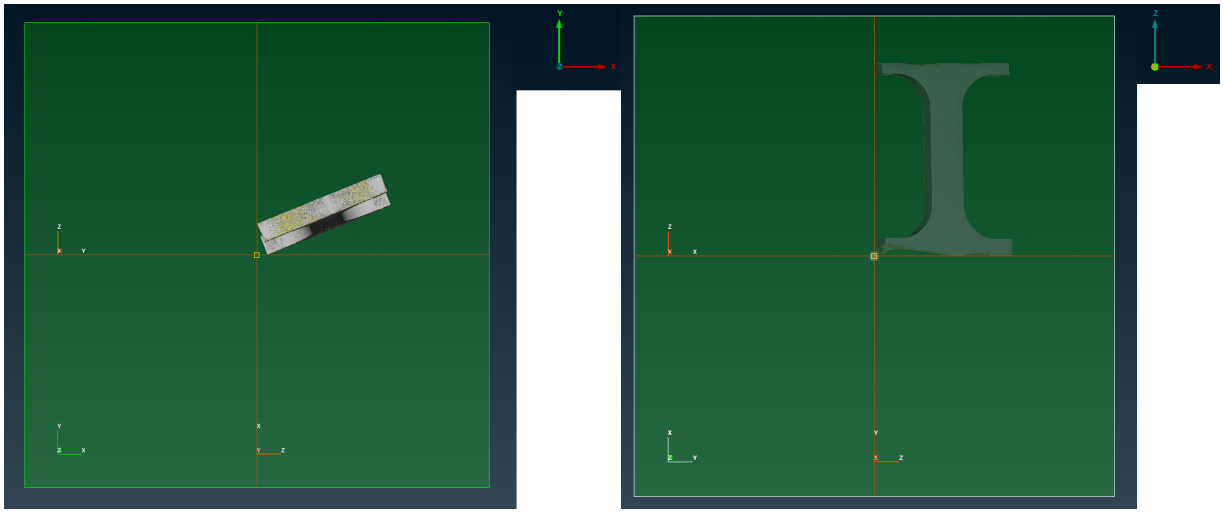

(a) The coupon in the x-y plane.

(b) The coupon in the x-z plane.

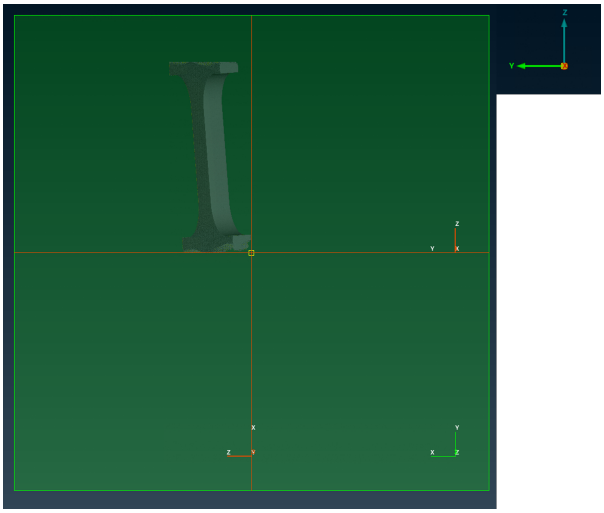

(c) The coupon in the y-z plane.

Figure A.1: The orientation of coupon 2-2 relative to the original XYZ planes when imported into ANSA.

DEPARTMENT OF INDUSTRIAL AND MATERIALS SCIENCE
CHALMERS UNIVERSITY OF TECHNOLOGY
Gothenburg, Sweden
www.chalmers.se

CHALMERS
UNIVERSITY OF TECHNOLOGY